

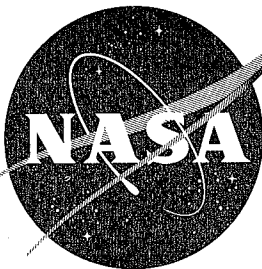
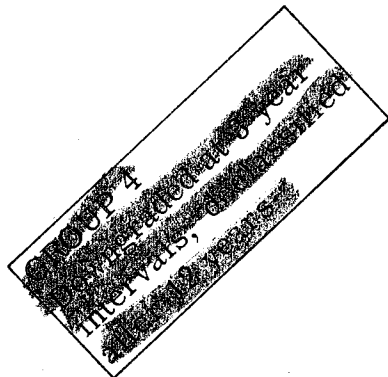
CONFIDENTIAL

Copy

NASA TM X-778

1-8-63

NASA TM X-778



CASE COPY FILE

TECHNICAL MEMORANDUM

X-778

STEADY AND FLUCTUATING PRESSURES AT TRANSONIC
SPEEDS ON HAMMERHEAD LAUNCH
VEHICLES

By Charles F. Coe and James B. Nute

Ames Research Center
Moffett Field, Calif.

*Approved for Release
by J. M. Howell
12-15-64*

CONFIDENTIAL

NATIONAL AERONAUTICS AND SPACE ADMINISTRATION

WASHINGTON

December 1962

CONFIDENTIAL

1
2
3
4
5
6
7
8
9
10
11
12
13
14
15
16
17
18
19
20
21
22
23
24
25
26
27
28
29
30
31
32
33
34
35
36
37
38
39
40
41
42
43
44
45
46
47
48
49
50
51
52
53
54
55
56
57
58
59
60
61
62
63
64
65
66
67
68
69
70
71
72
73
74
75
76
77
78
79
80
81
82
83
84
85
86
87
88
89
90
91
92
93
94
95
96
97
98
99
100

CONFIDENTIAL

NATIONAL AERONAUTICS AND SPACE ADMINISTRATION

TECHNICAL MEMORANDUM X-778

STEADY AND FLUCTUATING PRESSURES AT TRANSONIC

SPEEDS ON HAMMERHEAD LAUNCH

VEHICLES*

By Charles F. Coe and James B. Nute

SUMMARY

Steady and fluctuating pressures have been measured along the top center lines of three space-vehicle models with hammerhead-shaped profiles within the Mach number range from 0.60 to 1.17.

The results of the investigation showed that flow separation due to the hammerhead configuration can expose large areas of the vehicle to significant pressure fluctuations. The model with the largest hammerhead profile had the highest fluctuations due to separation and also the greatest length of significant unsteady flow. These relatively large fluctuations occur at subsonic speeds and can also occur at supersonic speeds if the ratio of diameters between the payload and following rocket stage is large. The intensities of the fluctuations in the region of the shock wave on the first-stage booster were increased when noticeable separation effects extended onto the interstage flare.

Measurements of representative power spectral densities of the fluctuations within the separated flow on the three models showed that the spectra were relatively flat over the measured range of frequencies.

*Title, Unclassified

UNCLASSIFIED

CONFIDENTIAL

INTRODUCTION

The unsteady aerodynamic loads associated with buffeting of vehicles during launch recently have become of considerable concern. These unsteady loads result from pressure fluctuations that occur within regions of shock waves or regions of separated flow or both. Results in references 1 and 2 suggest that much of the problem of buffeting could be eliminated if shapes of space-vehicle shrouds were selected judiciously. This option, however, is not always open to the designer since, for practical purposes, it is often necessary to use existing rocket components. In fact, it is the use of rocket stages which are smaller than their preceding payload stages that has led to the so-called hammerhead-shaped launch vehicles which can potentially have large regions of separated airflow.

Measurements of the steady and fluctuating pressures along the top center lines of three such hammerhead configurations are presented in this report. Two of the models were 10-percent scale of the nominal configurations of the Advent, and Ranger payload shrouds mounted on an Agena-Atlas booster combination. The models were bodies of revolution only and did not include detailed local protuberances or the full length of the Atlas.

The tests were conducted as part of a research program undertaken at Ames Research Center to investigate both the over-all buffet loads and the local steady and fluctuating pressures at transonic speeds on various body shapes. Model numbers of 11, 12, and 13 were assigned to the three models as part of the over-all test program numbering system, and were retained in this report to avoid later confusion of numbers. The results of the first phases of the investigation which illustrate the effects of some variations in launch vehicle nose shape are contained in references 1 and 2.

NOTATION

| | |
|--------------------------|--|
| C_p | time-average pressure coefficient, $\frac{p - p_o}{q_o}$ |
| $\Delta C_p(\text{RMS})$ | coefficient of the root-mean-square fluctuation of pressure about the mean |
| M | free-stream Mach number |
| Re | Reynolds number |
| p | local static pressure |
| p_o | free-stream static pressure |
| p_t | stagnation pressure |

CONFIDENTIAL

q_0 free-stream dynamic pressure
 α angle of attack

APPARATUS AND TECHNIQUE

Models

Profiles of the models tested are shown in figure 1. As can be seen in the photographs in figure 2, the models were bodies of revolution only, and thus did not include any detailed local protuberances. Also, the length of the Atlas booster was not scaled.

Sketches of the three models showing the pertinent dimensions and locations of the static-pressure orifices and pressure transducers are in figure 3. The orifice and transducer stations listed refer to model stations in inches from the noted location of the zero reference. The transducers were positioned on the top center line of the models and the static pressure orifices were offset $3/8$ inch to the right of the center line. The angular offset of the orifices was about 7.2° along the 6-inch-diameter Agena section of the models, but changed as the model radius varied. For convenience, the static pressures will be referred to as though they were measured along the top center lines of the models.


The three configurations tested were constructed to use a common main body which parted from the respective payload sections at station 30. All model parts were constructed of wood hollowed at the core to make room for the necessary transducer wires and pressure tubing. The payload sections and booster section were mated by means of an internal steel sleeve.

The semisolid wood models were considered to be rigid, and they also were rigidly mounted on the wind-tunnel sting support system. Although the flexibility of the sting support system permitted small motions of the model, tests in two different wind tunnels (ref. 1) showed that a change in tunnel support stiffness did not affect the root-mean-square values of the pressure fluctuations.

Wind Tunnel and Instrumentation

Tests were conducted in the Ames 14-Foot Transonic Wind Tunnel through a Mach number range from 0.60 to 1.17. The wind tunnel is a closed circuit except at an air exchanger which is controlled to maintain air temperature within certain operating limits. Because of the variation of stagnation temperature, Reynolds number varies with Mach number as illustrated by the shaded band in figure 4.

The pressure transducers and electronic components that recorded the pressure fluctuations were the same as in reference 1 with one exception. In the root-mean-square recording circuit, a filter which eliminated frequencies above the linear-response range of the transducers was changed from 6 to 12 decibels per octave. An amplitude response curve showing the applied band-pass filtering is



in figure 5. The curve indicates the range of frequencies represented by the pressure fluctuation measurements presented in this report.

The 0.250-inch diameter transducers were mounted flush. The back side of the diaphragm of each transducer was referenced to the time-average static pressure from its adjacent orifice so that the transducers responded only to the fluctuations of pressure about the mean. A combined tube length of approximately 150 feet connected the transducer and its adjacent orifice outside of the tunnel at the manometers which recorded the static pressures. This arrangement not only assured a steady reference pressure but facilitated the calibration of the transducers.

PROCEDURE

The calibration and data-reduction methods were the same as those described in reference 1. The tests were conducted within the range of angles of attack from -4° to $+8^{\circ}$. The Mach number was varied within the test limits from 0.60 to 1.17. In the range of Mach numbers where significant pressure fluctuations occurred in the regions of the normal shock waves ($0.7 < M < 0.95$), the Mach number was adjusted in whatever increments were required to locate the maximum intensities at pressure transducers. In the figures containing these data, the locations of potential peaks between stations have been indicated by dashed lines.


During most of the tests a transition strip was located on the nose cones of the models as shown in the photographs of figure 2. The basic tests of model 13 were conducted without the transition strip; however, some repeat tests were made with the transition strip to determine its effect on both the fluctuating and steady pressure measurements.

RESULTS AND DISCUSSION

Intensities of Pressure Fluctuations

The longitudinal distributions of pressure fluctuations as measured on the top center lines of the three models are presented in figures 6, 7, and 8. As noted in references 1 and 2, fluctuations in two types of flow regions exist on hammerhead-shaped payload stages. First, there are the regions of flow expansions followed by shock waves in which there are extremely local but relatively high pressure fluctuations; for example, at station 20.2, figure 6(a), $M = 0.80$. Second, there are regions of separated flow in which potentially large areas may be subjected to unsteady flow, as in figure 6(a), between stations 22 and 40. This separation of flow is probably of greatest concern when the effects of the hammerhead payload on buffeting are considered.

As would be expected, model 11 having the largest ratio of body diameters and a body convergence angle of 34° had the highest fluctuations due to separation and also the greatest length of significant unsteady flow (fig. 6). There were sizable fluctuations at supersonic Mach numbers for this model whereas, for the smaller



ratios of body diameter, the fluctuations became insignificant at Mach numbers above 1. Reference 2 indicates that separation effects are negligible at supersonic Mach numbers for a ratio of diameters as large as that of model 11 if the body convergence angle is small. From this result it may appear desirable to use a small body convergence angle on a hammerhead configuration. It is important, however, to consider other factors in addition to the occurrence of pressure fluctuations. Some unpublished results obtained as part of this over-all research program have shown, for example, that motion effects can be dynamically destabilizing to the aerodynamic loads for certain profiles with relatively low body convergence angles.


The fluctuations in the regions of the shock waves, which occur as locally concentrated peaks, can be seen in figures 6 and 8 on both the payload fairings and on the boosters downstream of their cone-cylinder intersections. Comparison of the peak pressure fluctuation intensities on the booster section of the models shows that the fluctuations were highest with the payload fairing of model 11. For this configuration, it can be seen that significant fluctuations extended from the "boattail" section onto the interstage flare.

The effect of fixing transition on the nose cone of model 13 can be noted in figure 8(b) for $M = 0.89$. The results which are representative of those obtained indicate an insignificant effect.

Steady Pressures

The longitudinal distributions of the steady pressures along the top center line of the models are shown in figures 9, 10, and 11, for selected Mach numbers illustrative of the range of the tests. Results obtained at $\alpha = -4^\circ$ have been plotted with the $\alpha = 4^\circ$ data to represent the equivalent of the bottom center-line pressures. As was the case with the pressure fluctuations, the presence of the transition strip on model 13 had negligible effect on the static pressures (fig. 11(a)).

As indicated in references 1 and 2, some relationship between steady and fluctuating pressures is apparent. The locations of the maximum fluctuations in regions of shock waves can always be determined, for example, from the position of the steep rising pressure gradients through the shock waves. Comparisons of fluctuating pressures in figures 6, 7, and 8, with the steady pressures in figures 9, 10, and 11, also show that regions of fluctuations due to separation can usually be located from the static pressure distributions and a knowledge of the body profile. Figure 12 shows some representative comparisons of steady and fluctuating pressures to illustrate the relationship. Fluctuations due to separation began on the hammerhead configurations at the break in model contour where the body converges or in the region of the static pressure rise through the shock wave when it preceded the break as in figure 12(c), $M = 0.89$. It can be seen that the fluctuations reach maximum values where the pressure gradients in the separated regions were large and that they diminished as the static pressure distributions approached a constant free-stream static pressure. It is interesting to note that for models 11 and 13 the maximum fluctuations in the separated



CONFIDENTIAL

regions occurred at some distance downstream of the break in model contour that caused the separation.

Power Spectral Densities

Representative power spectral densities of the pressure fluctuations within the separated flow on each of the models are shown in figure 13. The flat spectra obtained are typical for separated flow regions.

Ames Research Center
National Aeronautics and Space Administration
Moffett Field, Calif., Aug. 23, 1962

REFERENCES

1. Coe, Charles F.: Steady and Fluctuating Pressures at Transonic Speeds on Two Space-Vehicle Payload Shapes. NASA TM X-503, 1961.
2. Coe, Charles F.: The Effects of Some Variations in Launch-Vehicle Nose Shape on Steady and Fluctuating Pressures at Transonic Speeds. NASA TM X-646, 1962.



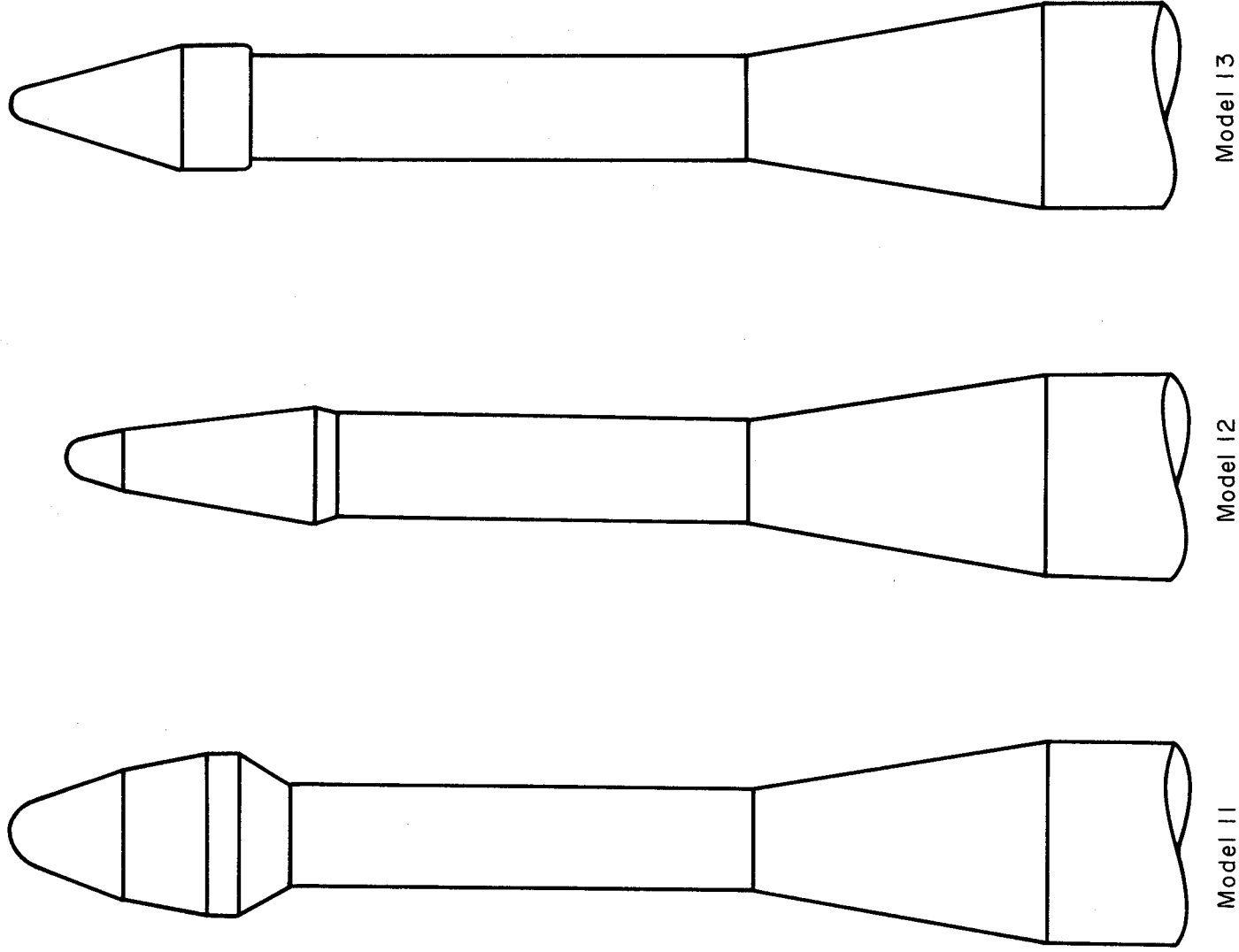
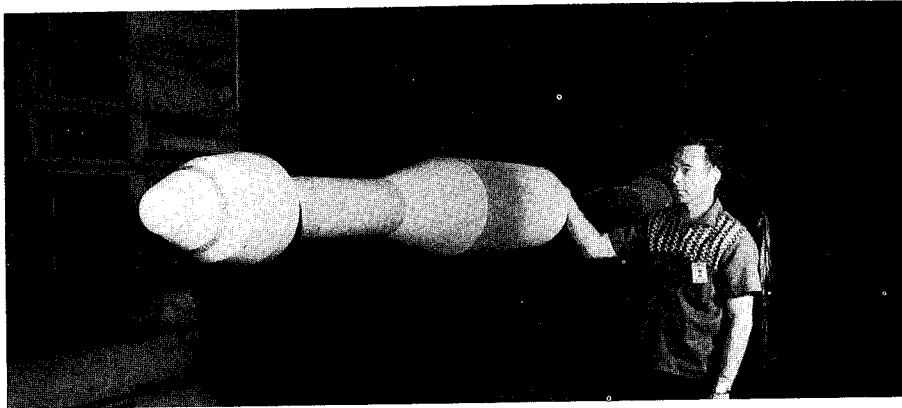
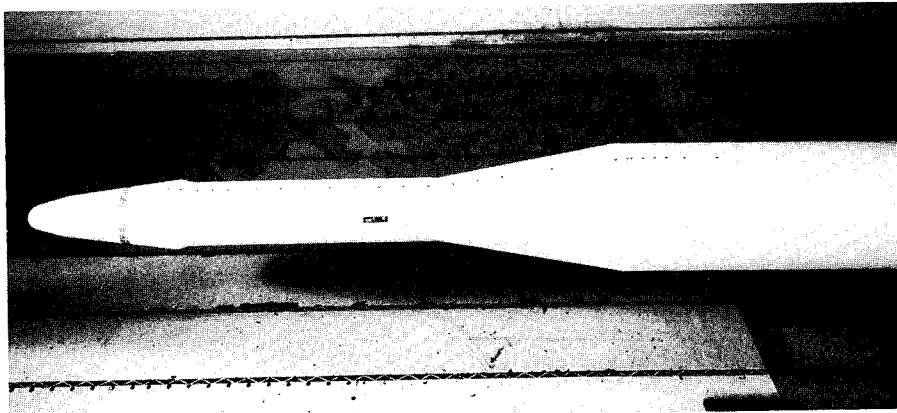


Figure 1.- Profiles of models tested.

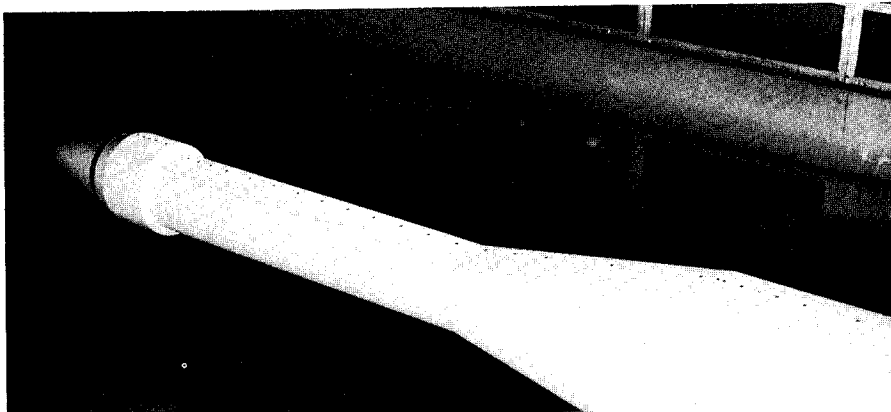
~~CONFIDENTIAL~~



Model 11



Model 12



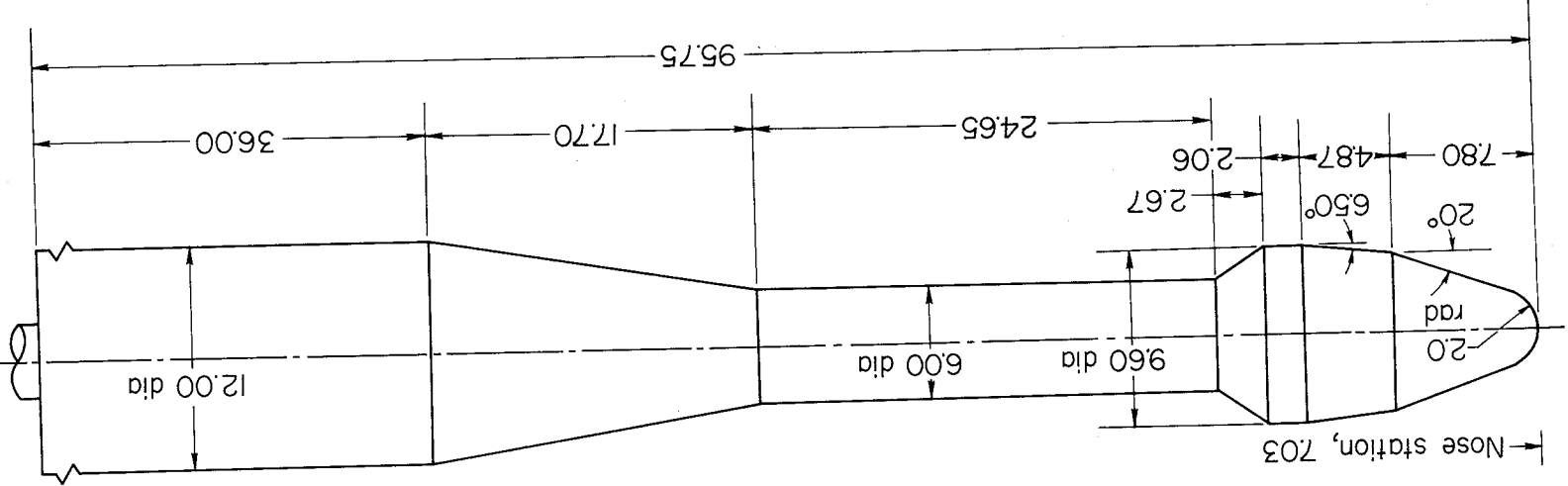
Model 13

Figure 2.- Photographs of the models.



CONFIDENTIAL

| Pressure orifice stations, inches | Pressure transducer stations |
|-----------------------------------|------------------------------|
| 848 | |
| 995 | |
| 114 | |
| 128 | |
| 142 | |
| 152 | |
| 167 | |
| 191 | |
| 202 | |
| 212 | |
| 226 | |
| 239 | |
| 256 | |
| 271 | |
| 286 | |
| 312 | |
| 336 | |
| 360 | |
| 384 | |
| 408 | |
| 432 | |
| 456 | |
| 480 | |
| 504 | |
| 528 | |
| 552 | |
| 576 | |
| 600 | |
| 630 | |
| 660 | |
| 671 | |
| 675 | |
| 686 | |
| 697 | |
| 708 | |
| 725 | |
| 756 | |
| 780 | |
| 804 | |
| 829 | |
| 852 | |

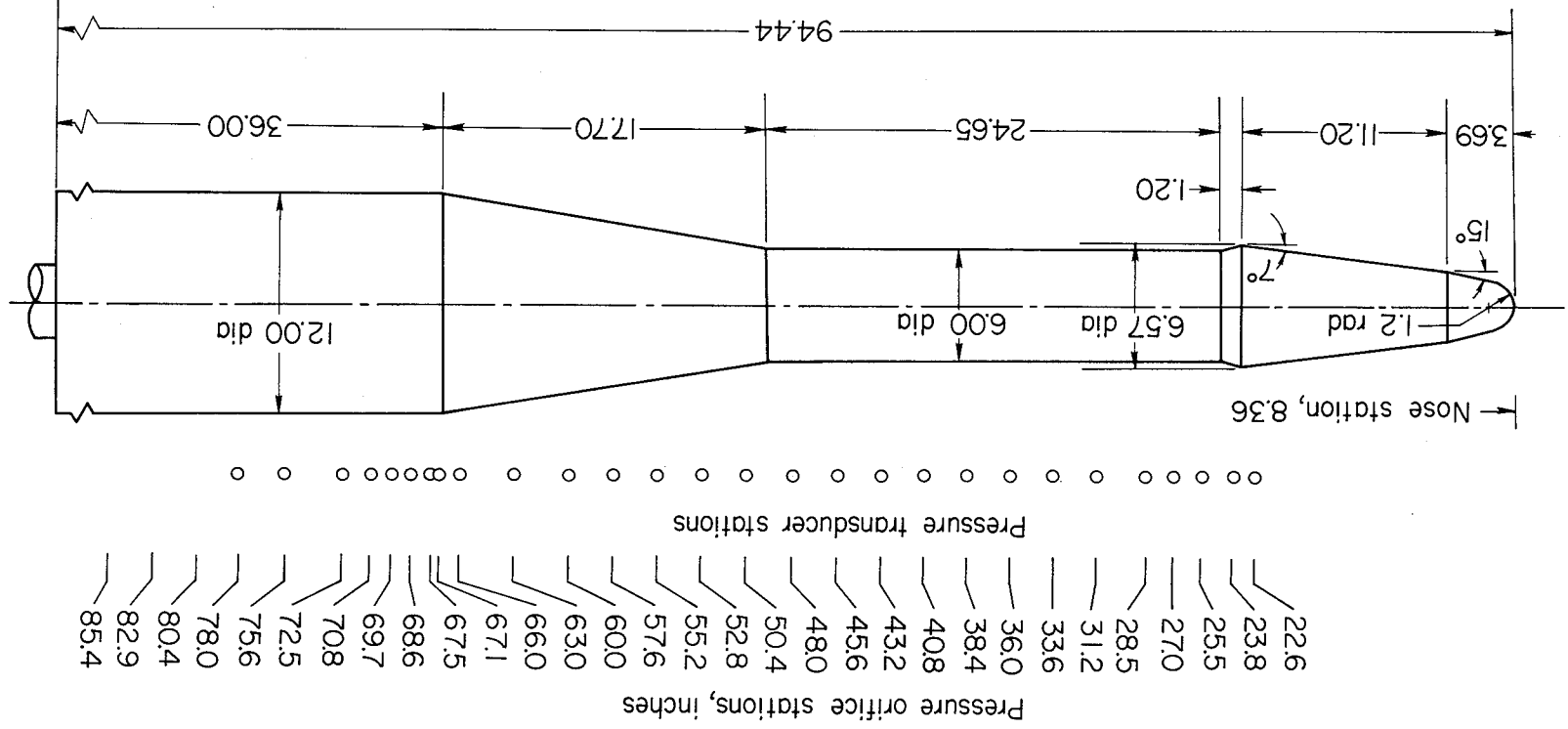


NOTE: All dimensions in inches.

(a) Model 11

Figure 3.- Sketches of models showing pertinent dimensions and locations of the static-pressure orifices and pressure transducers.

CONFIDENTIAL



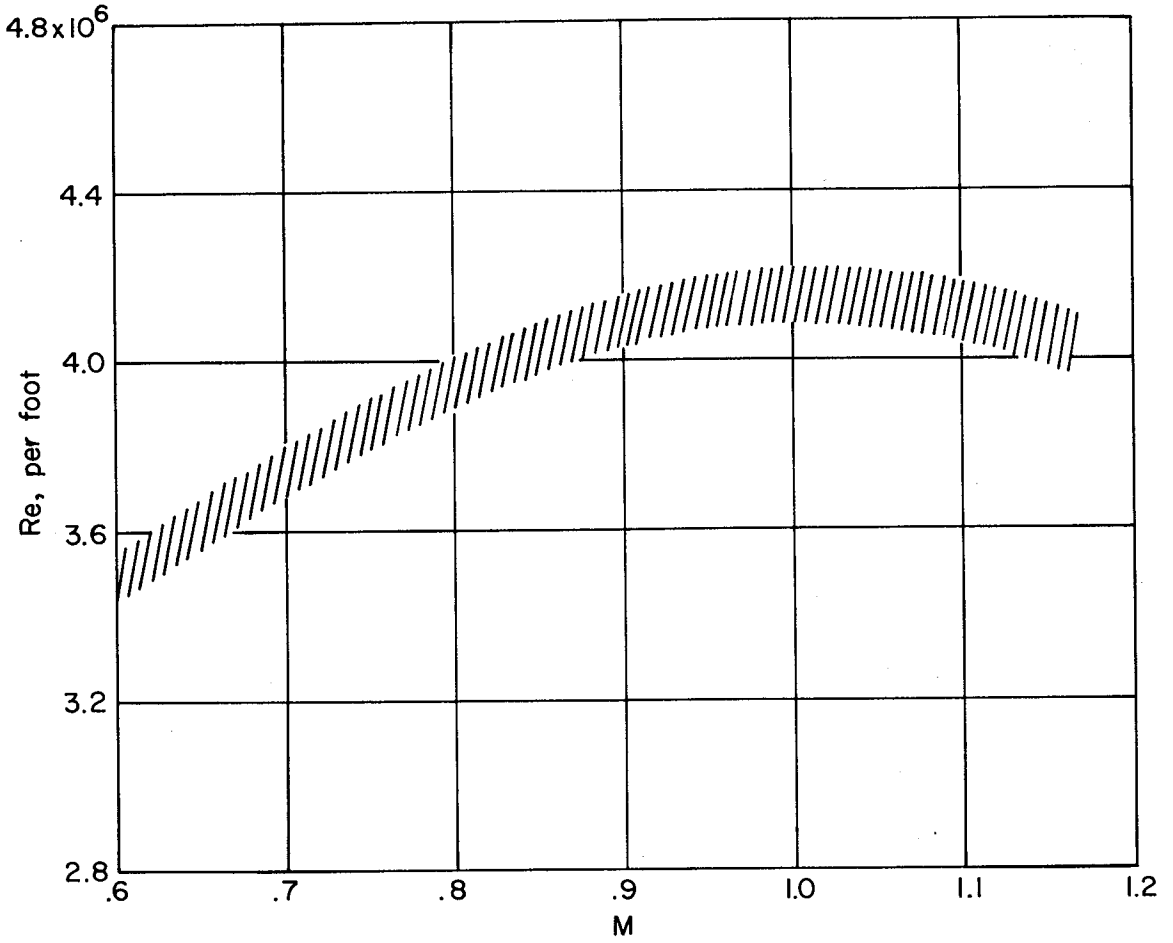


Figure 4.- Reynolds number range of the tests.



CONFIDENTIAL

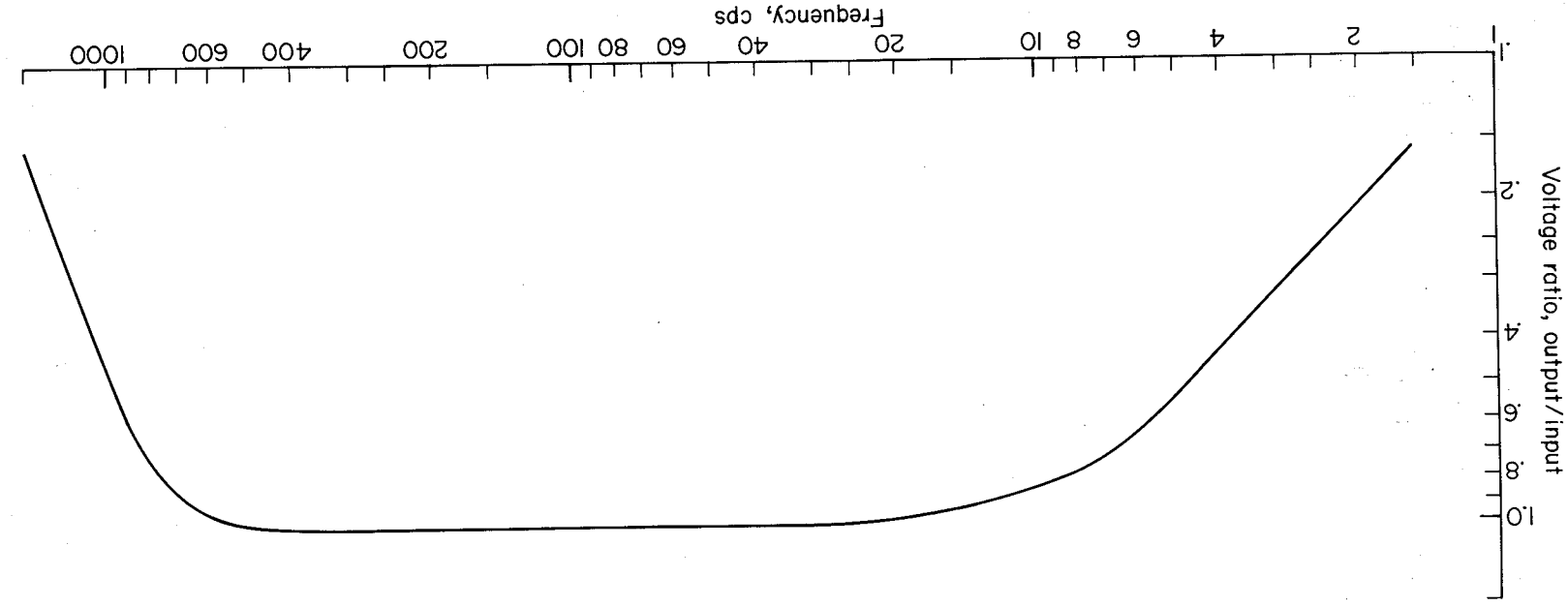
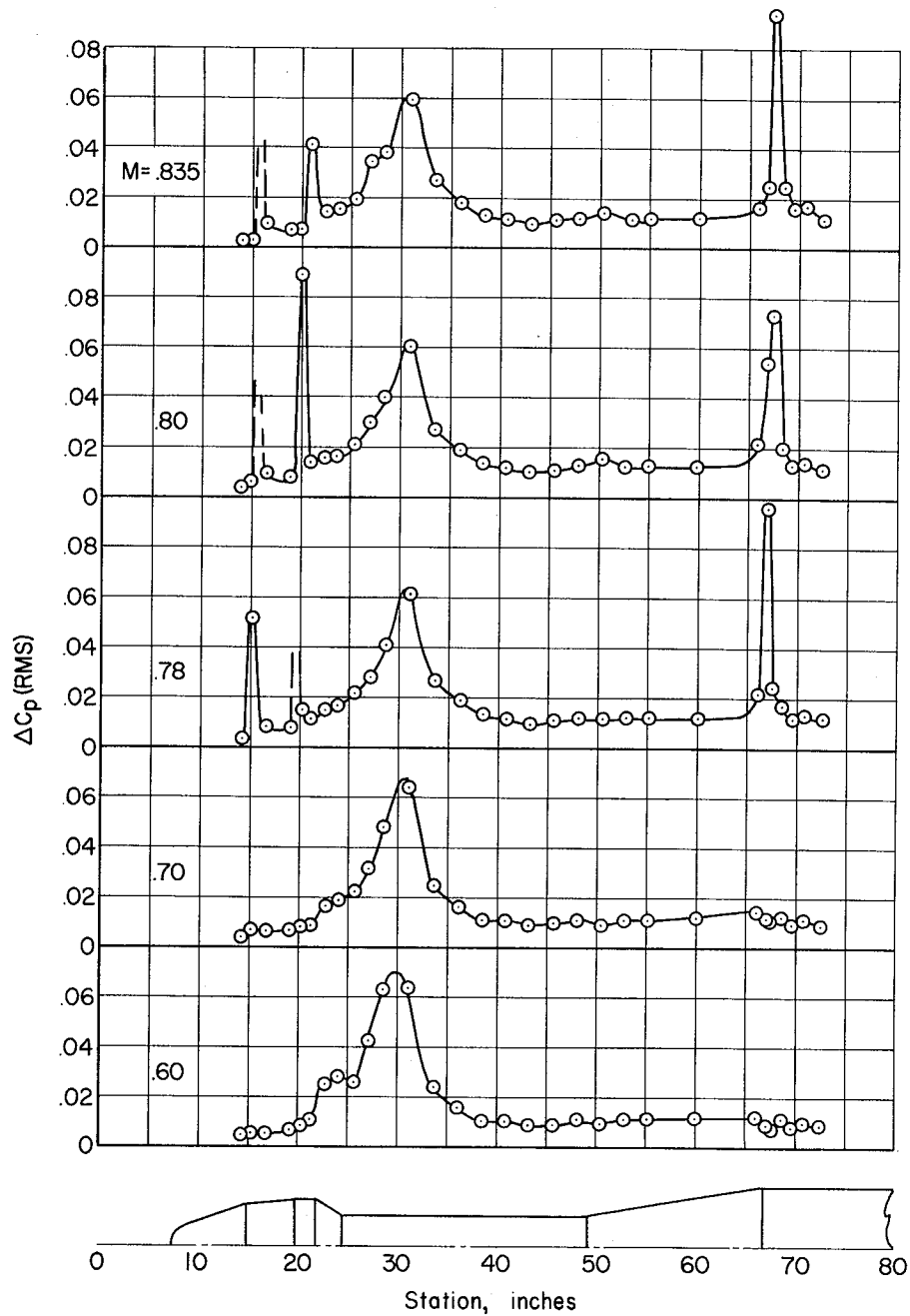
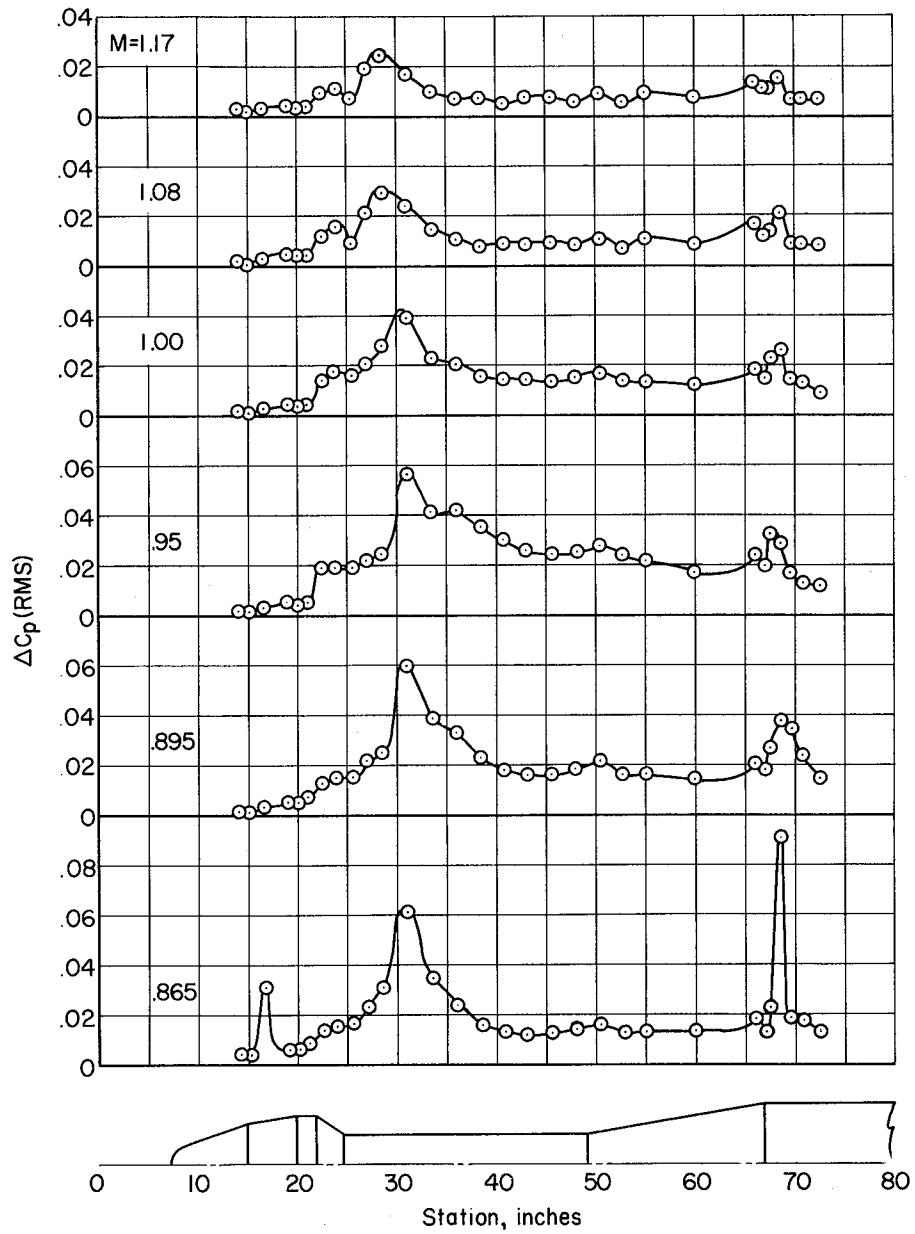


Figure 5.- Amplitude response of band-pass filtering applied to the root-mean-square measurements.



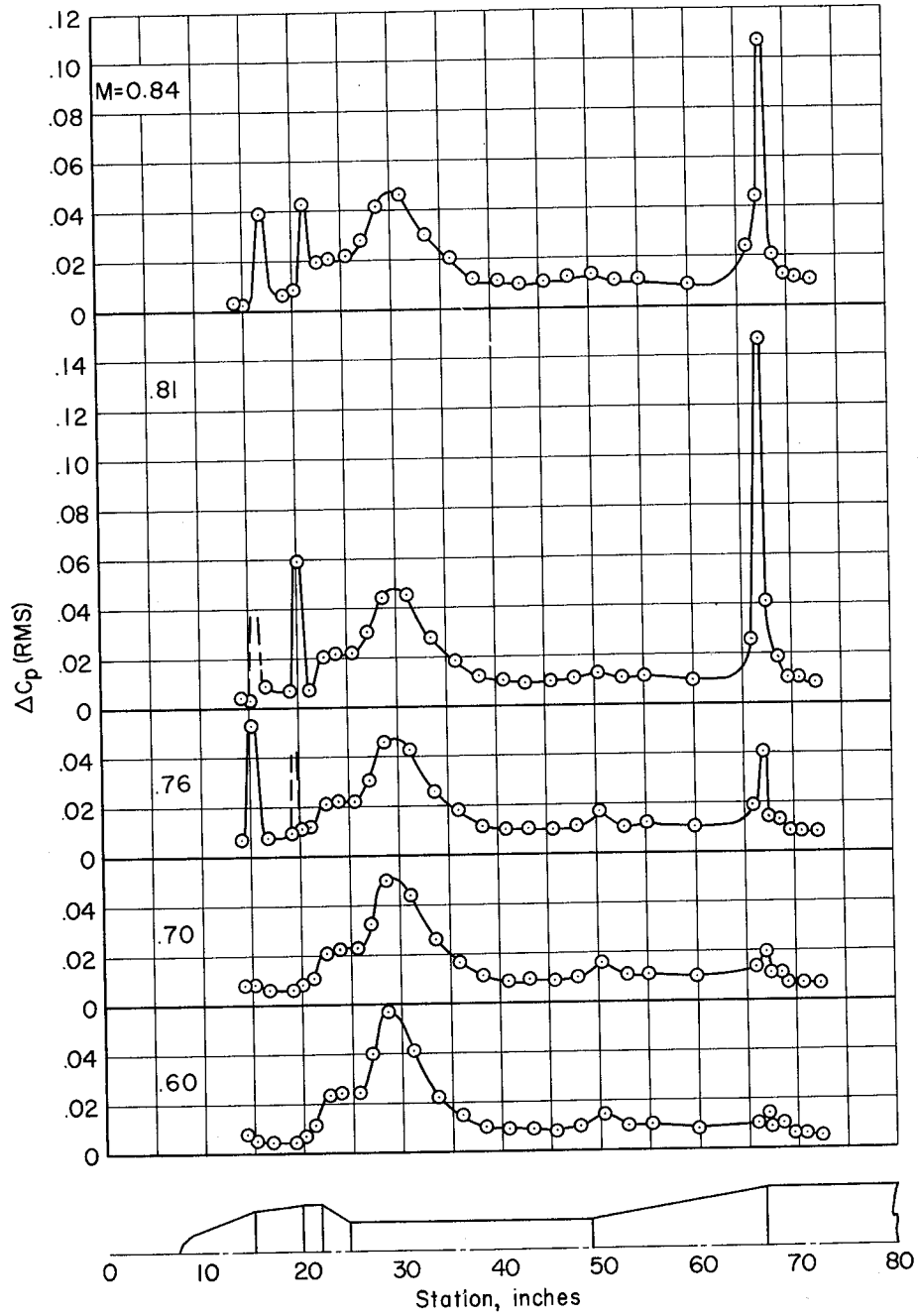
(a) $\alpha = -4^\circ$

Figure 6.- Longitudinal distribution of the pressure fluctuations on model 11.



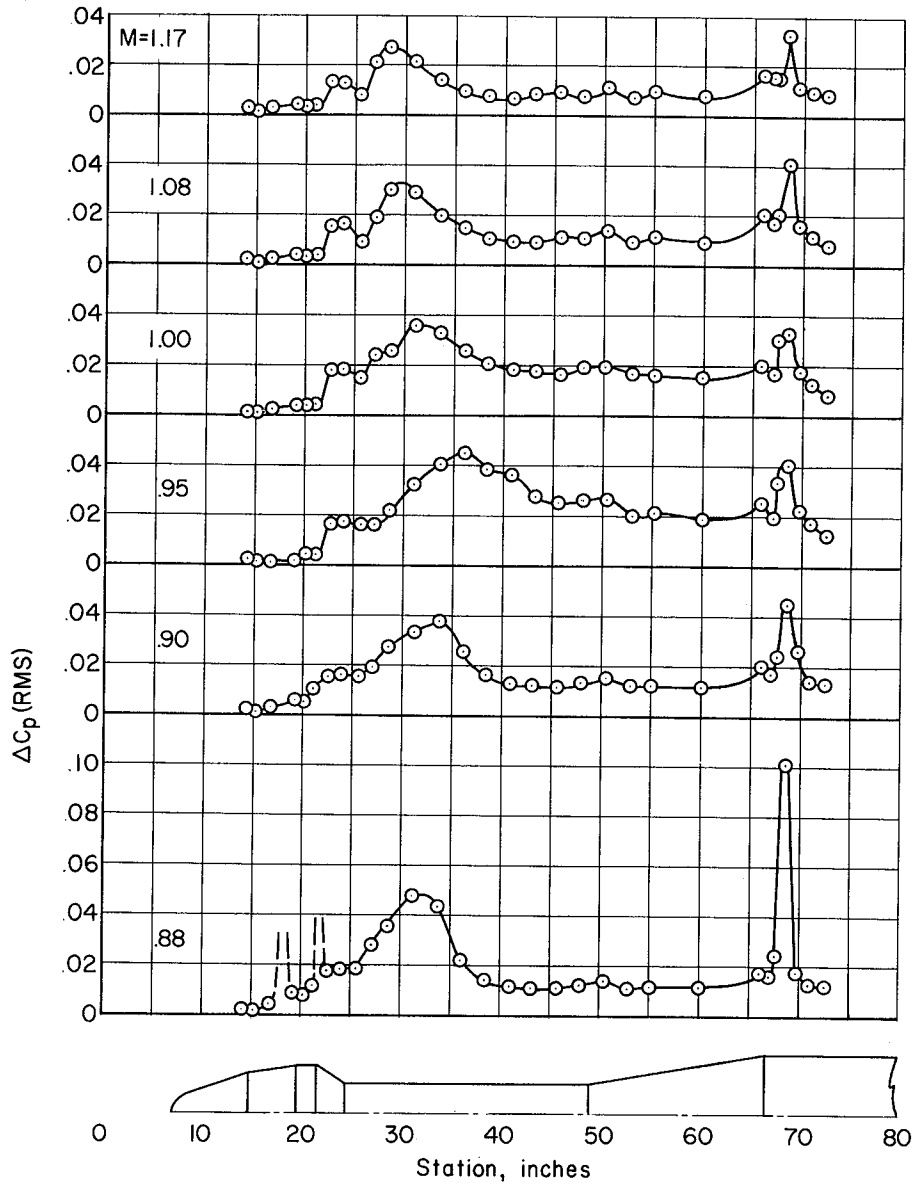
(a) $\alpha = -4^\circ$ - Concluded.

Figure 6.- Continued.



(b) $\alpha = 0^\circ$

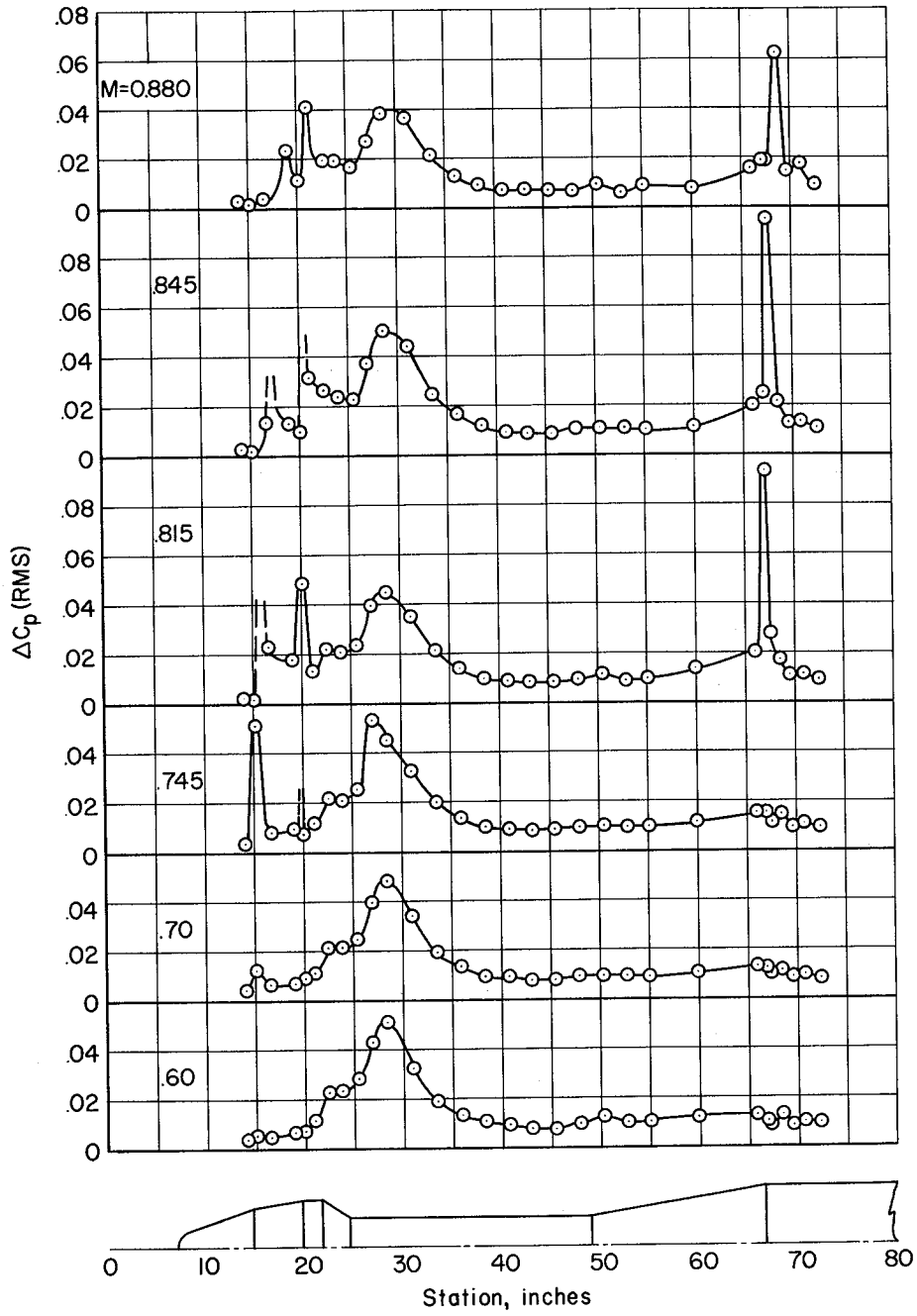
Figure 6.- Continued.



(b) $\alpha = 0^\circ$ - Concluded.

Figure 6.- Continued.

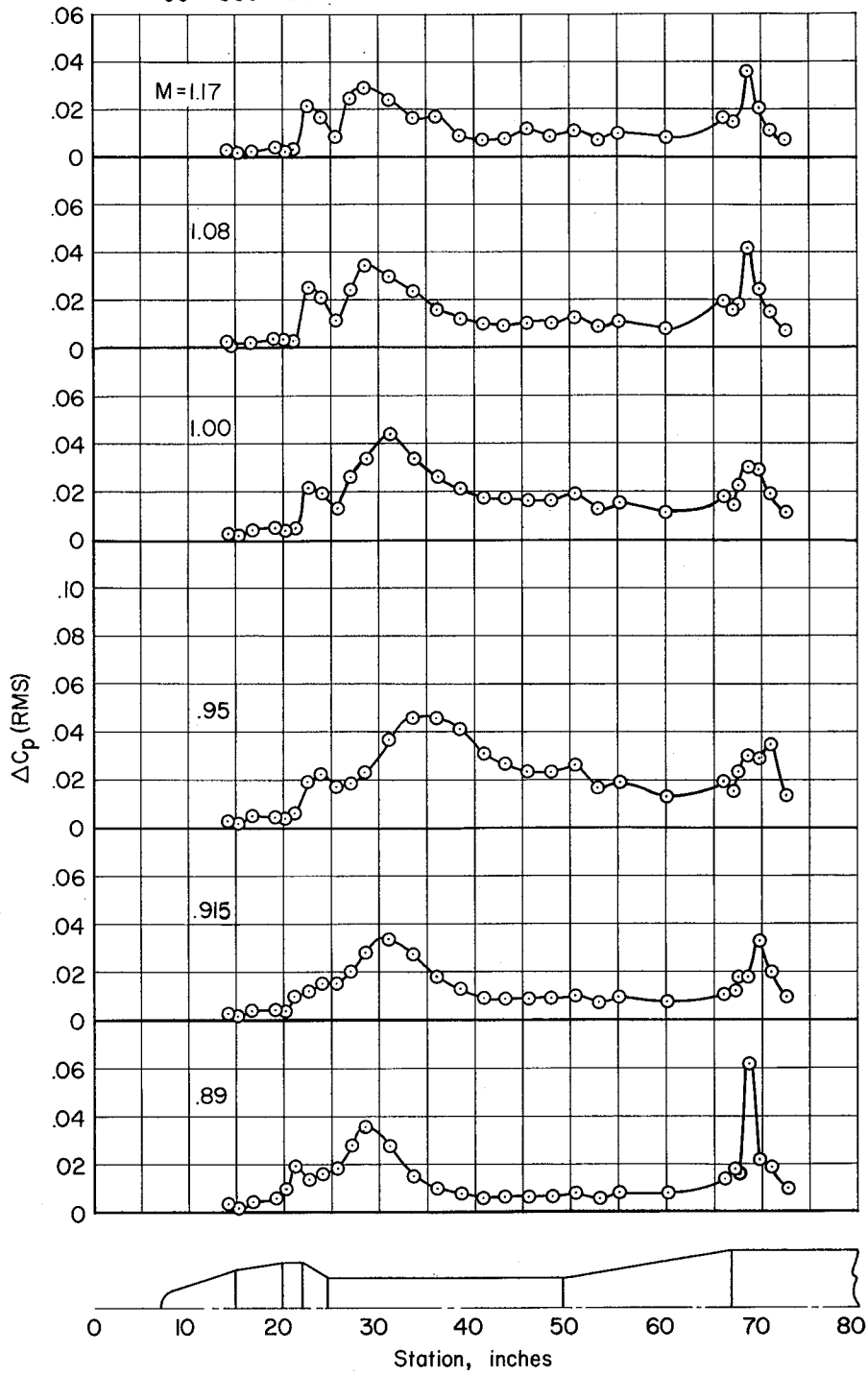
C [REDACTED]



(c) $\alpha = 4^\circ$

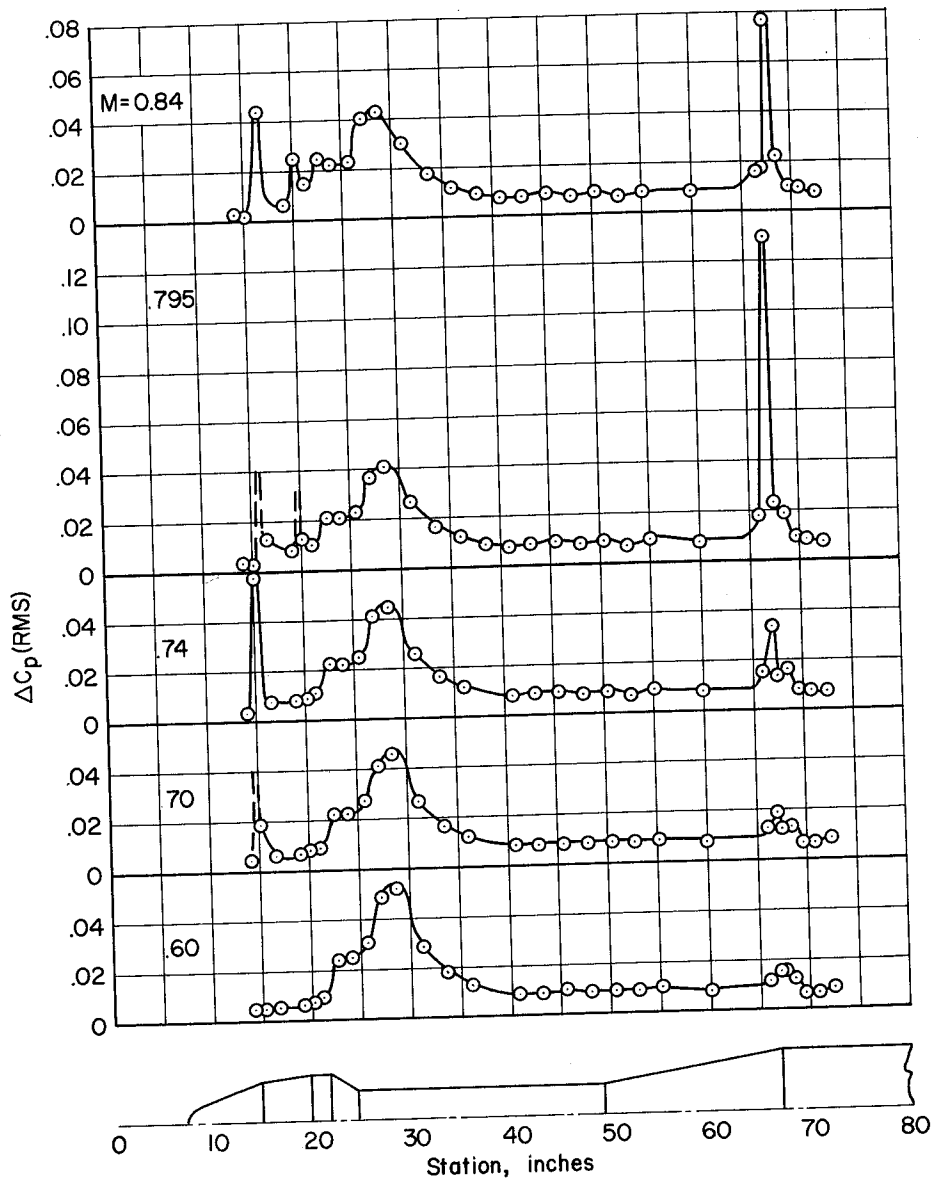
Figure 6.- Continued.





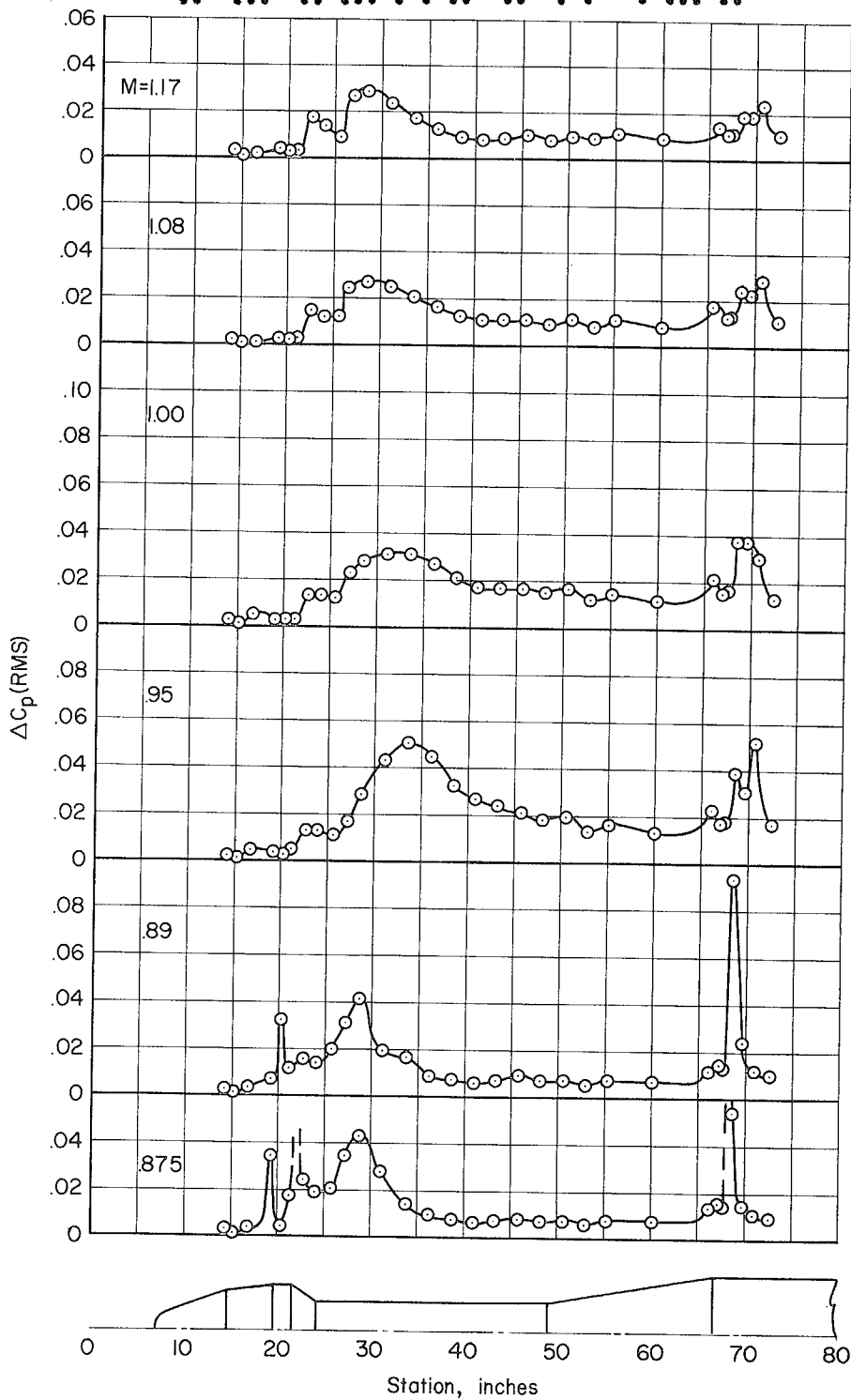
(c) $\alpha = 4^\circ$ - Concluded.

Figure 6.- Continued.



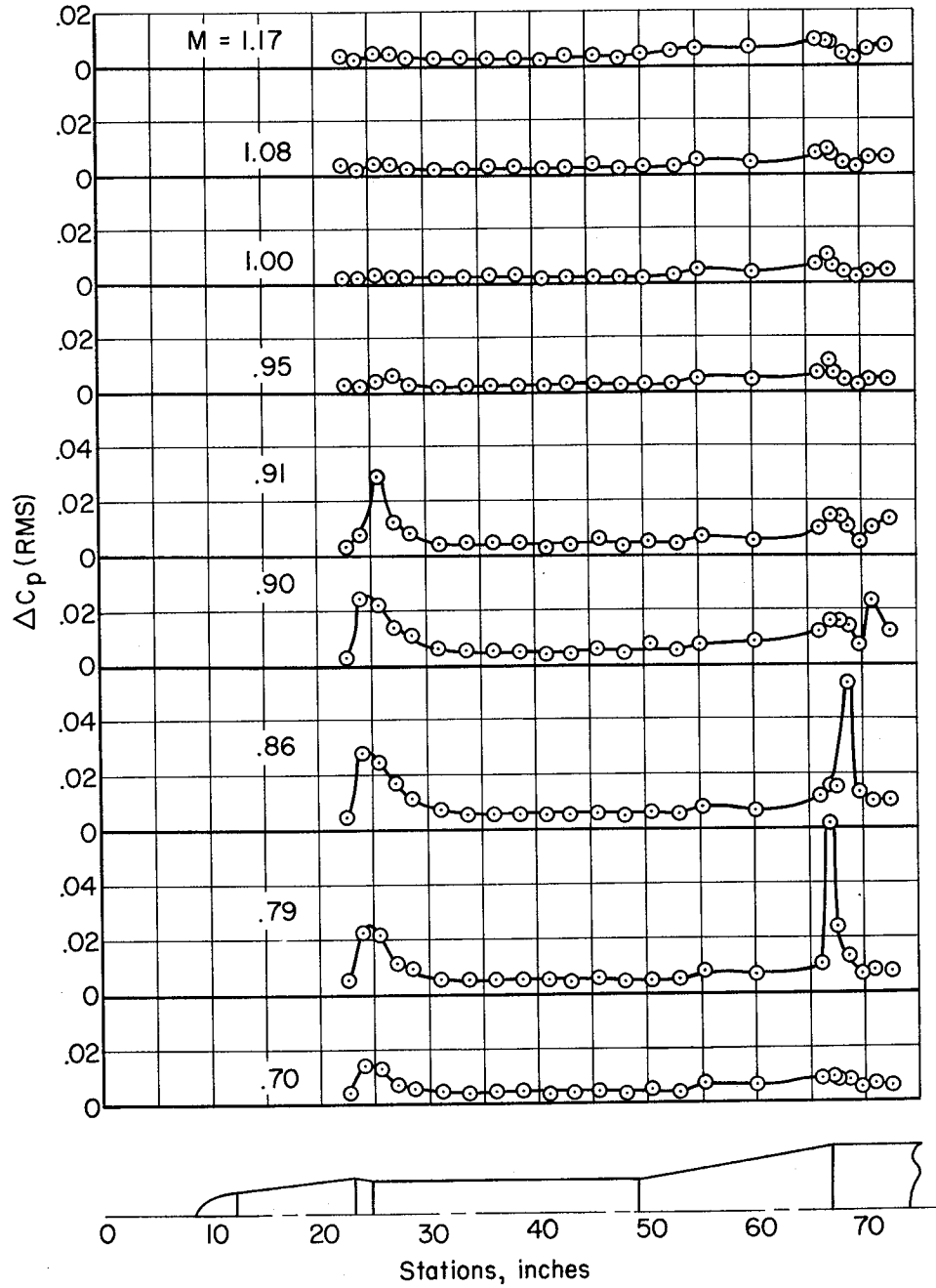
(d) $\alpha = 8^\circ$

Figure 6.- Continued.



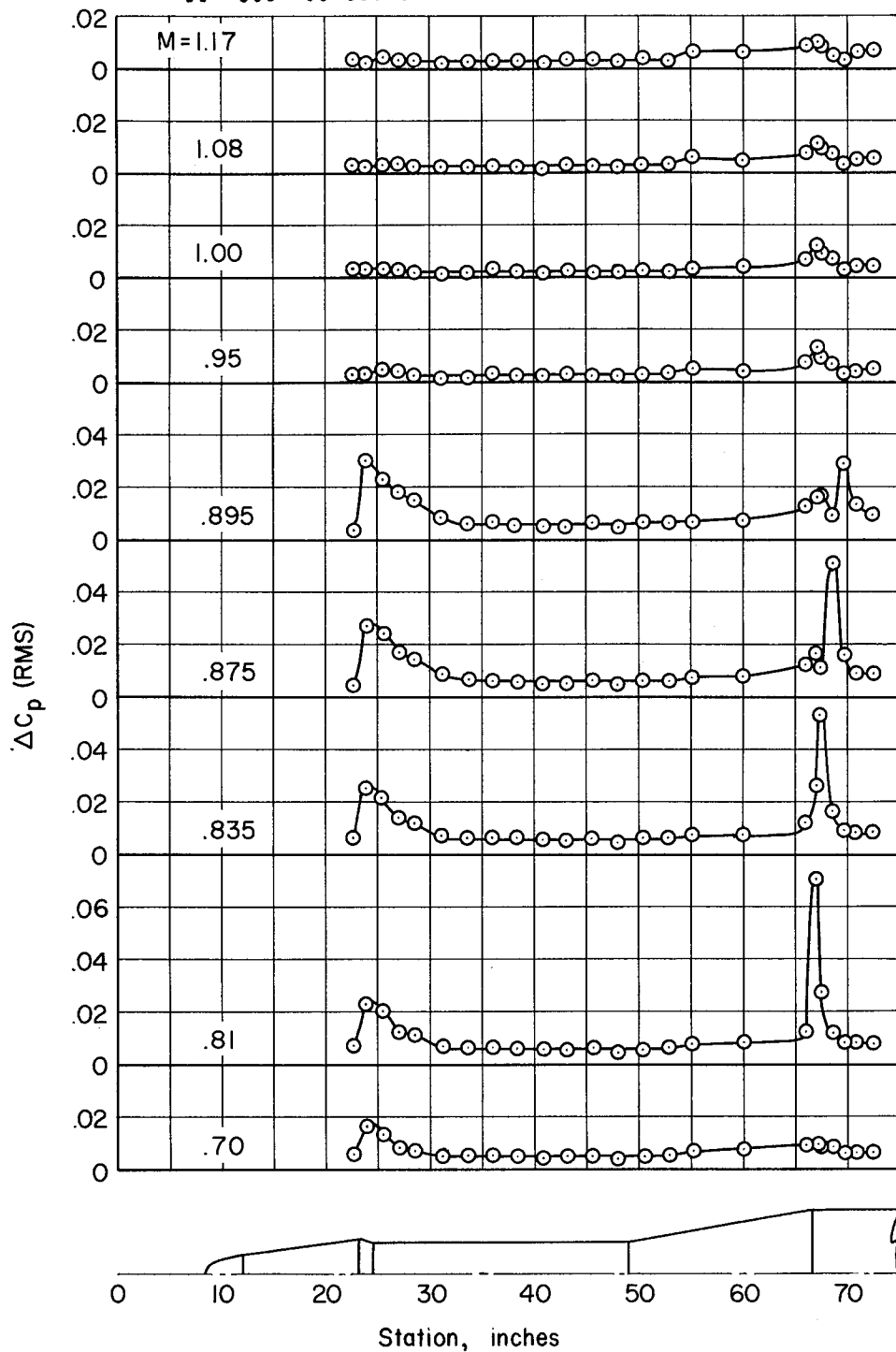
(d) $\alpha = 8^\circ$ - Concluded.

Figure 6.- Concluded.



(a) $\alpha = 0^\circ$

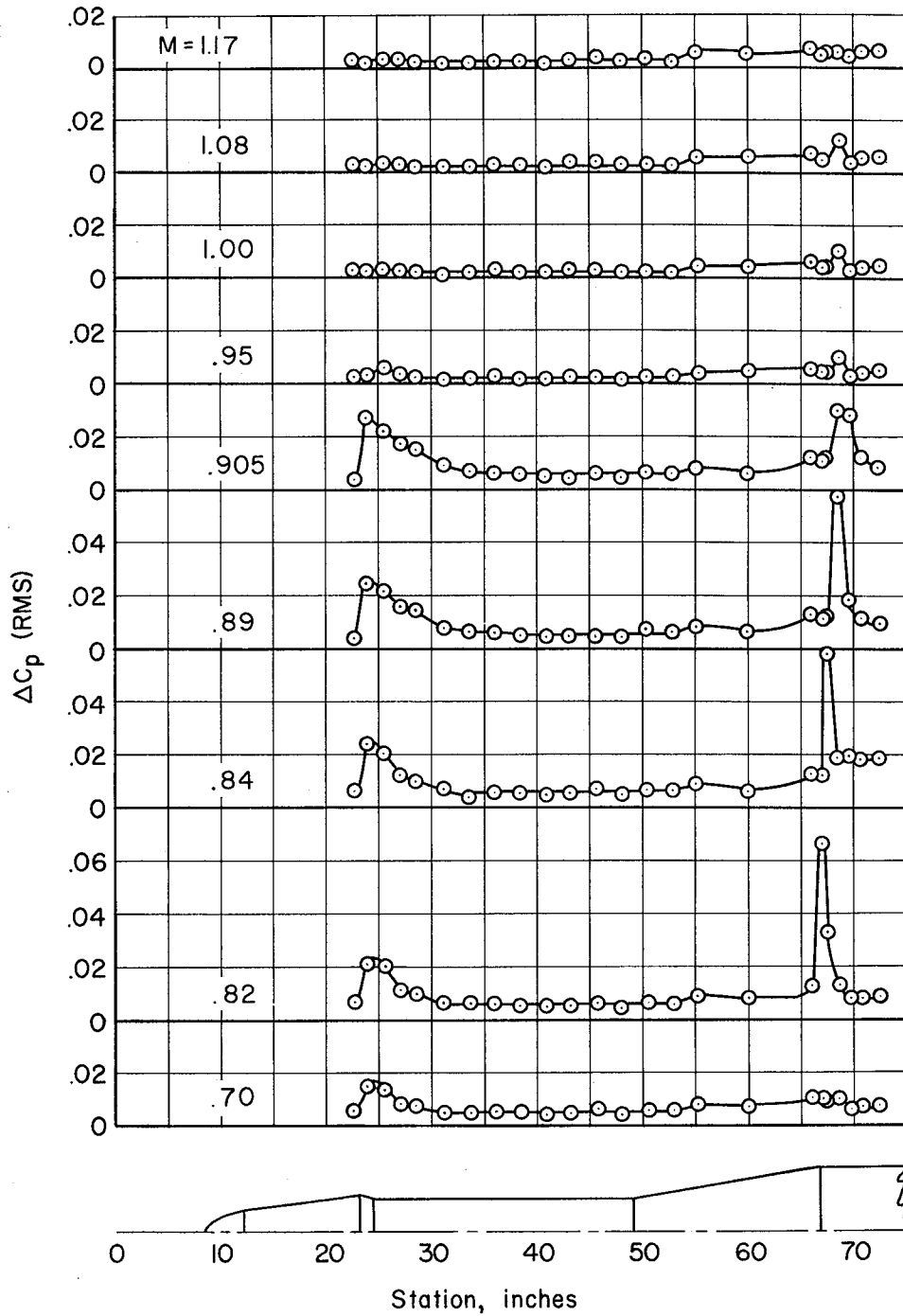
Figure 7.- Longitudinal distribution of the pressure fluctuations on model 12.



(b) $\alpha = 4^\circ$

Figure 7.- Continued.



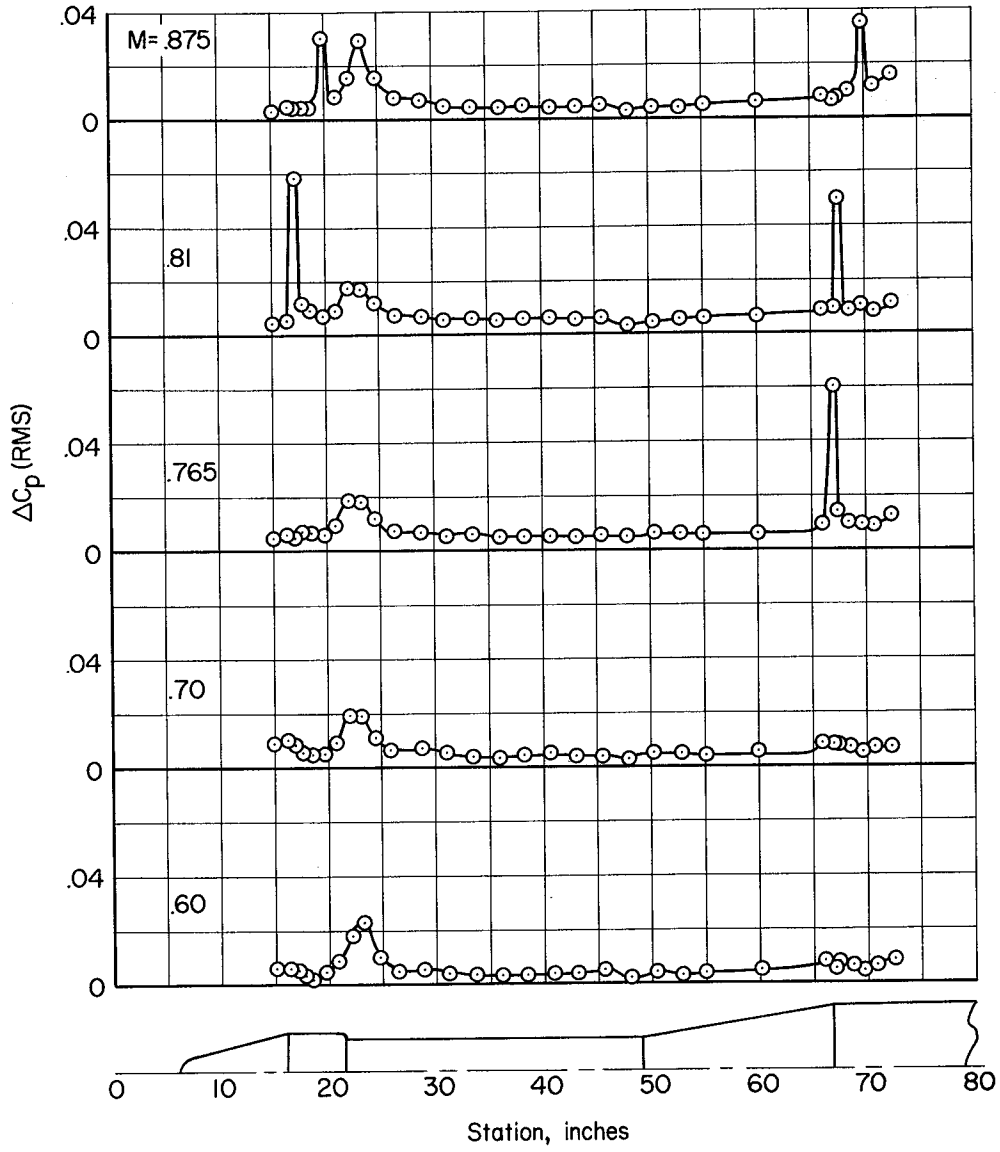


(c) $\alpha = 8^\circ$

Figure 7.- Concluded.

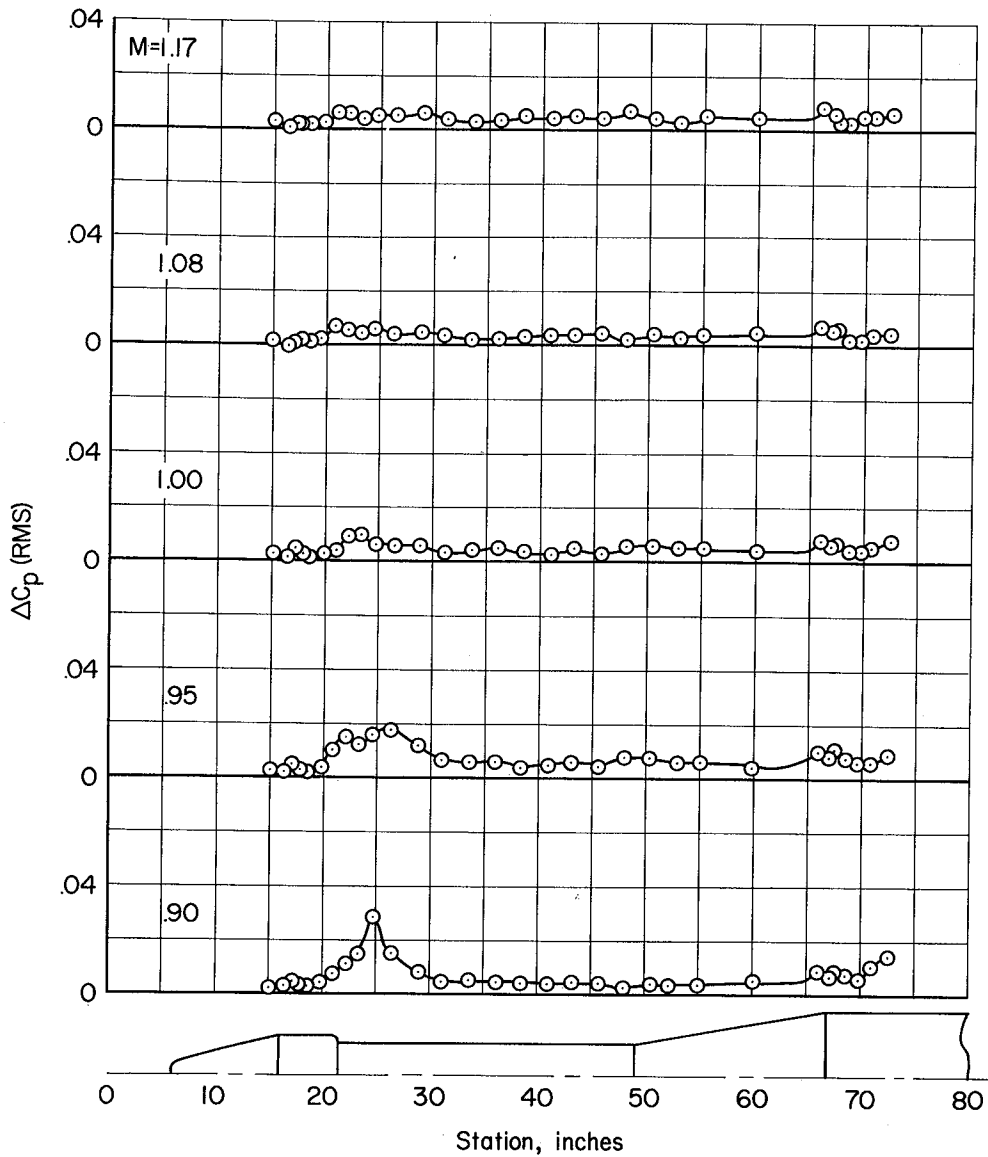
DECLASSIFIED





(a) $\alpha = -4^\circ$

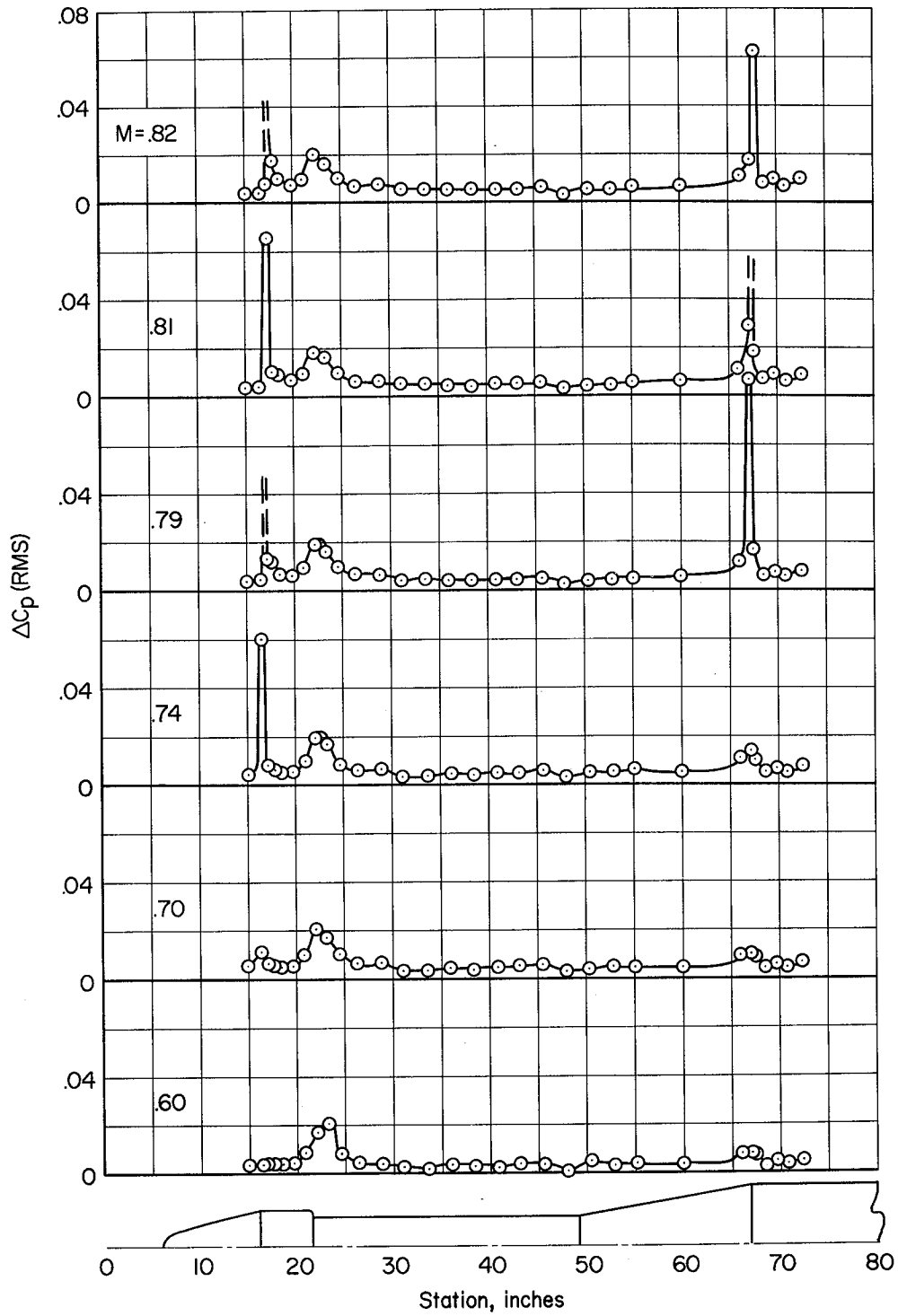
Figure 8.- Longitudinal distribution of the pressure fluctuations on model 13.



(a) $\alpha = -4^\circ$ - Concluded.

Figure 8.- Continued.

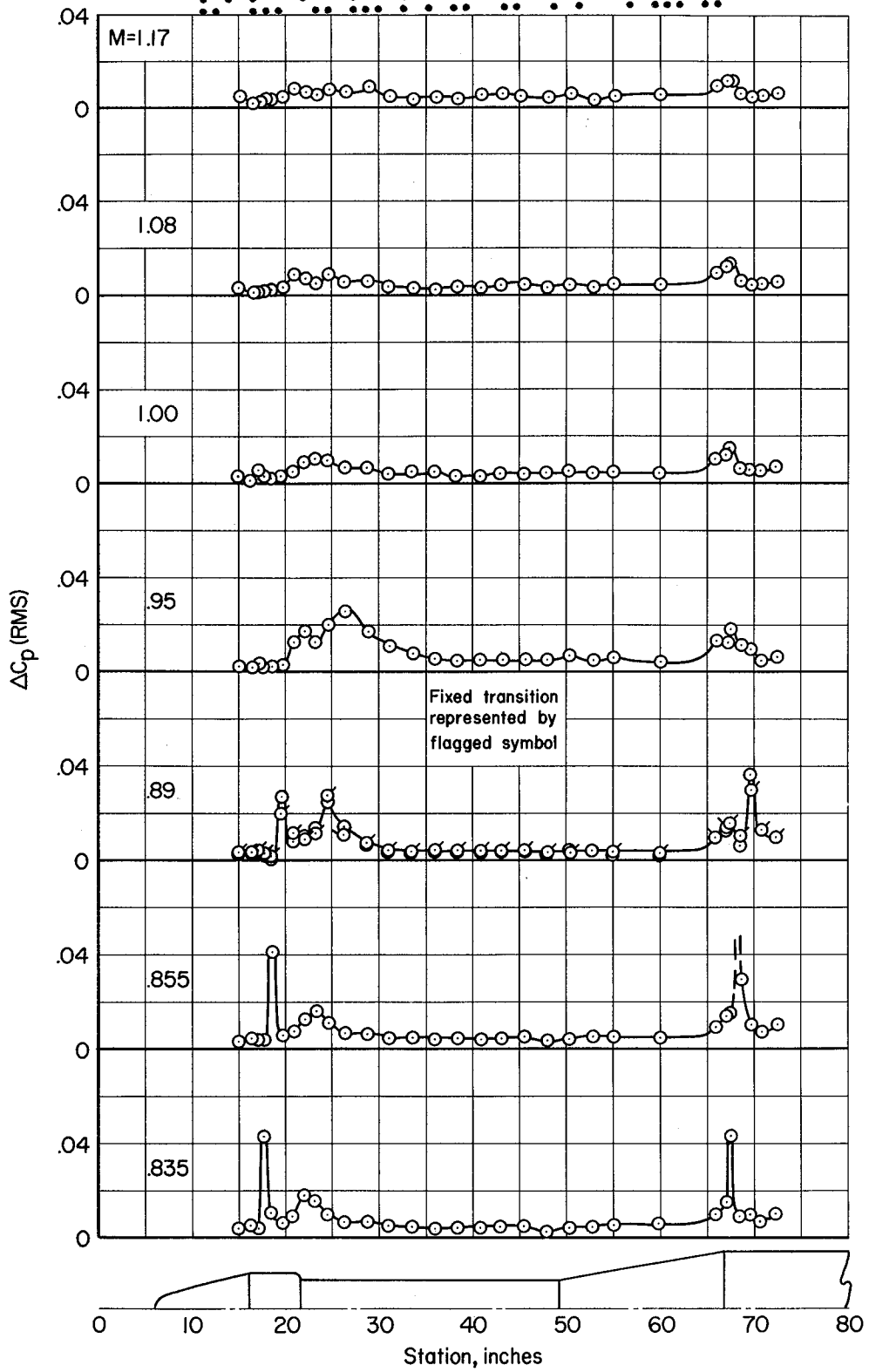




(b) $\alpha = 0^\circ$

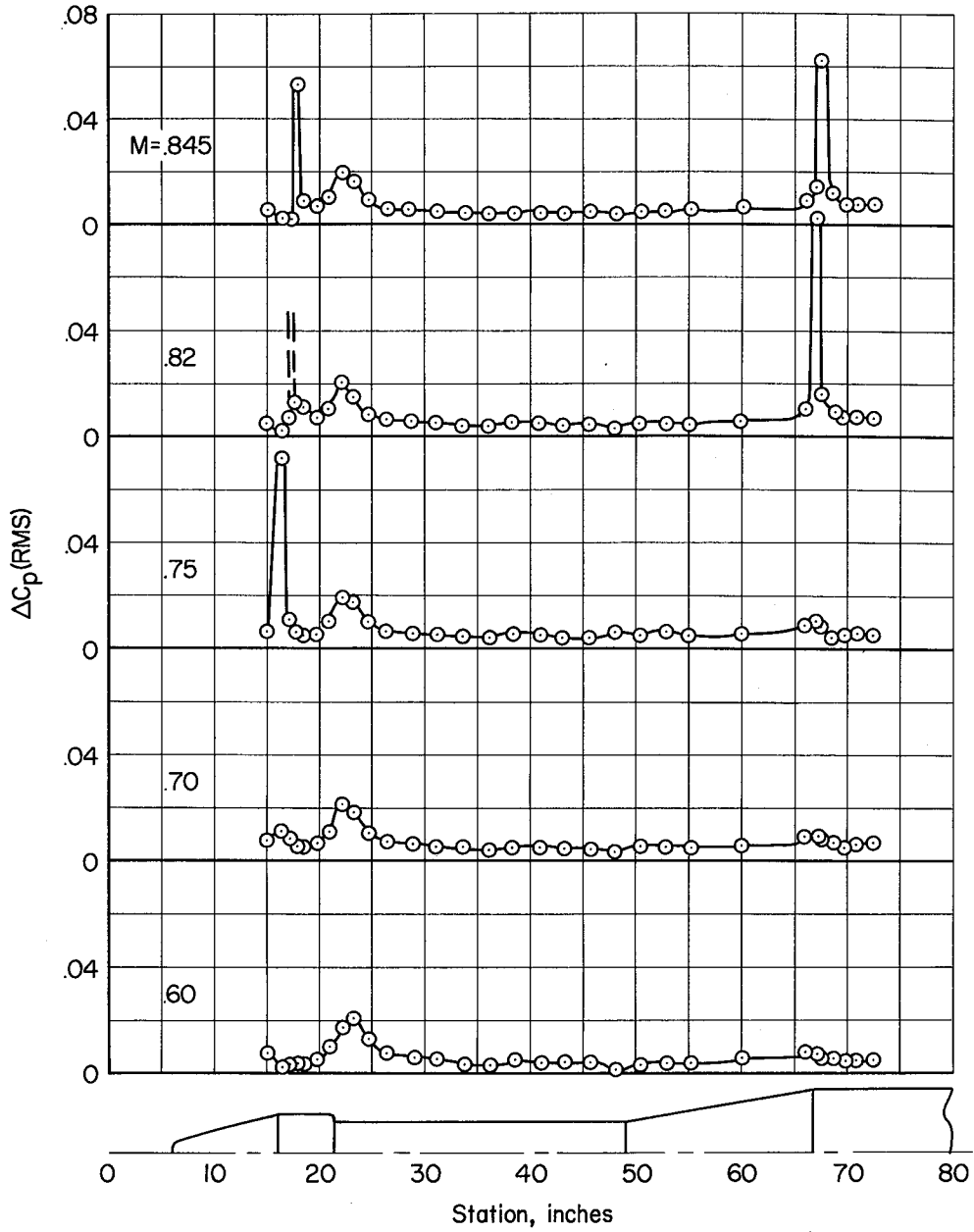
Figure 8.- Continued.





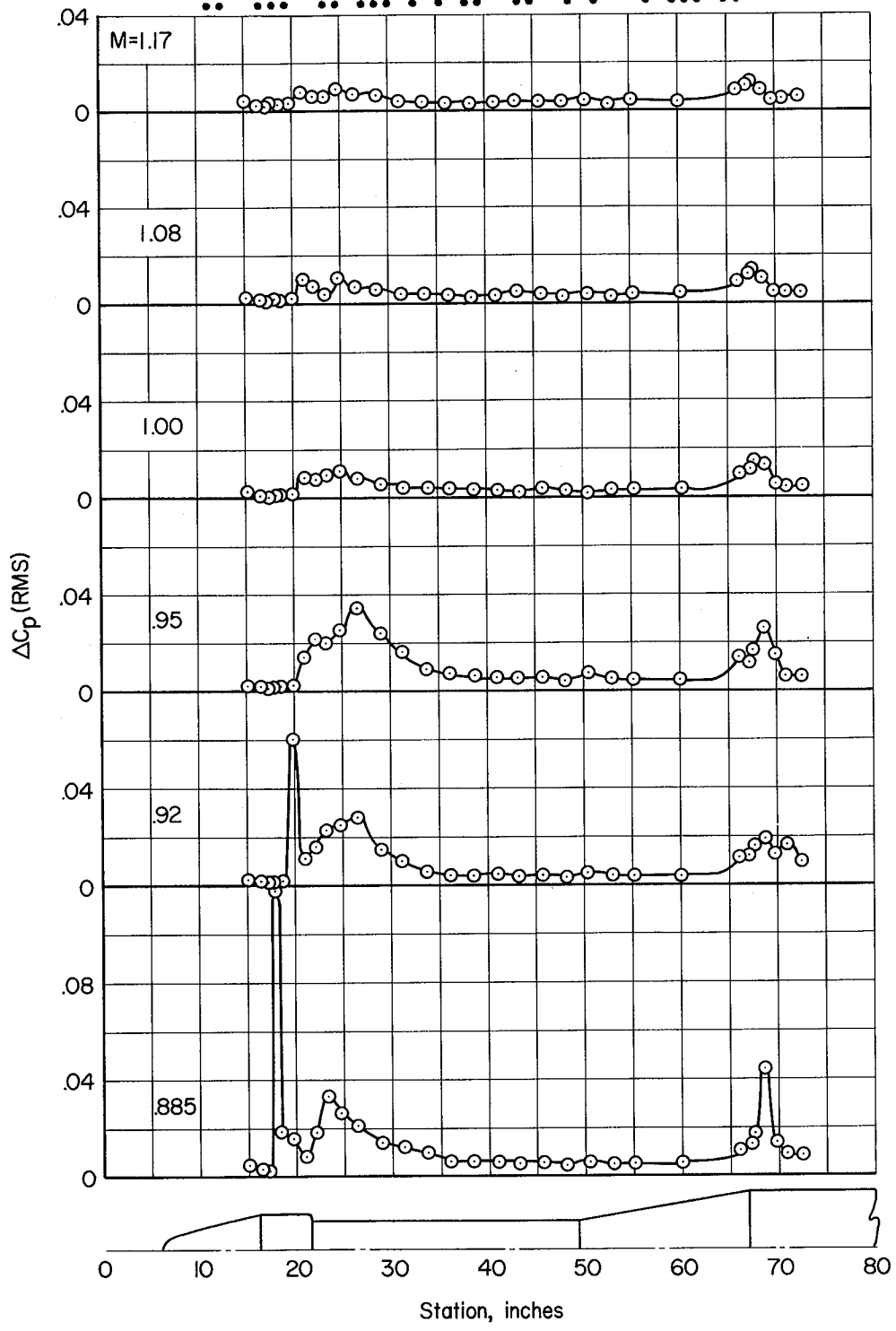
(b) $\alpha = 0^\circ$ - Concluded.

Figure 8.  inued.



(c) $\alpha = 4^\circ$

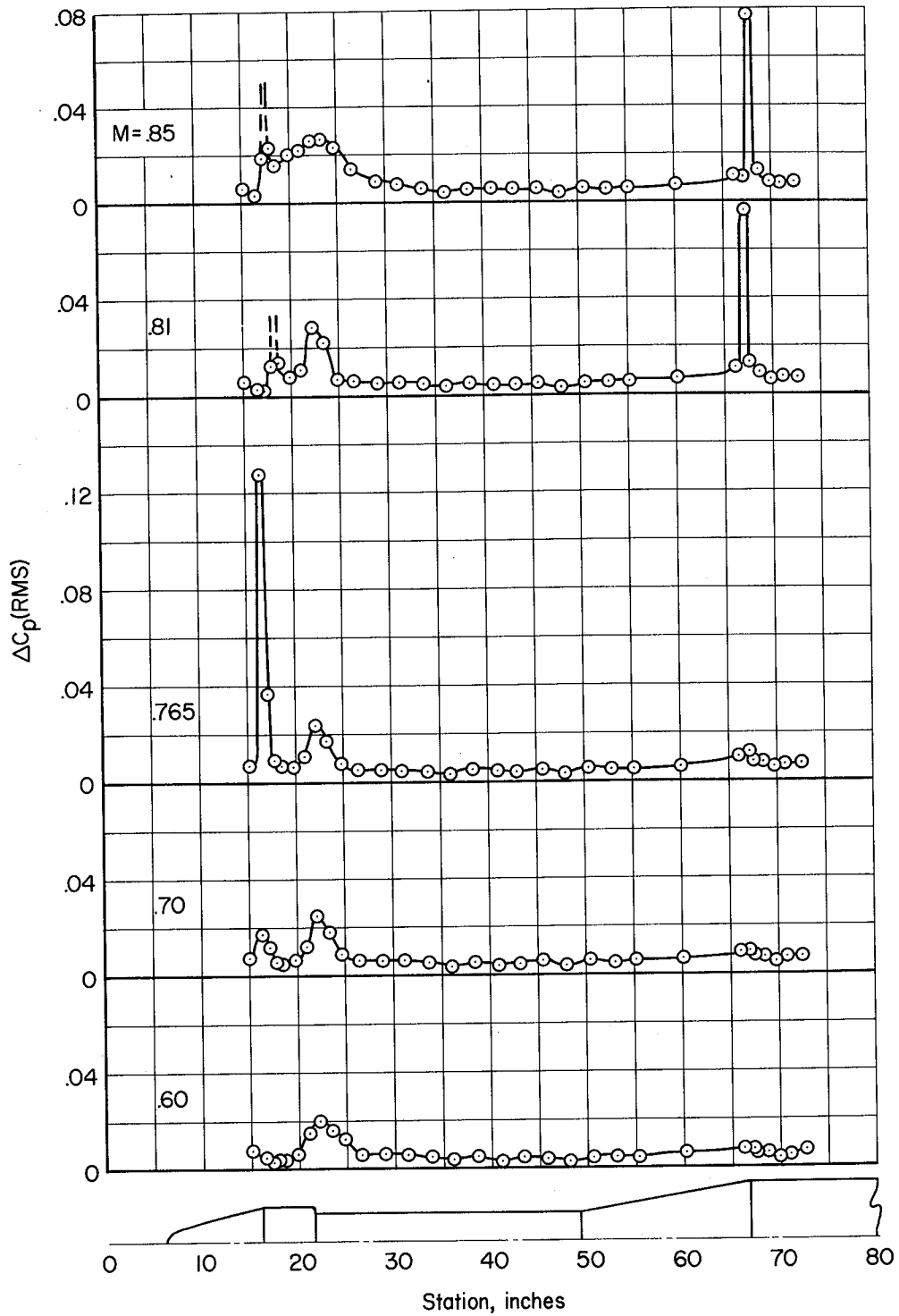
Figure 8.- Continued.



(c) $\alpha = 4^\circ$ - Concluded.

Figure 8.- Continued.

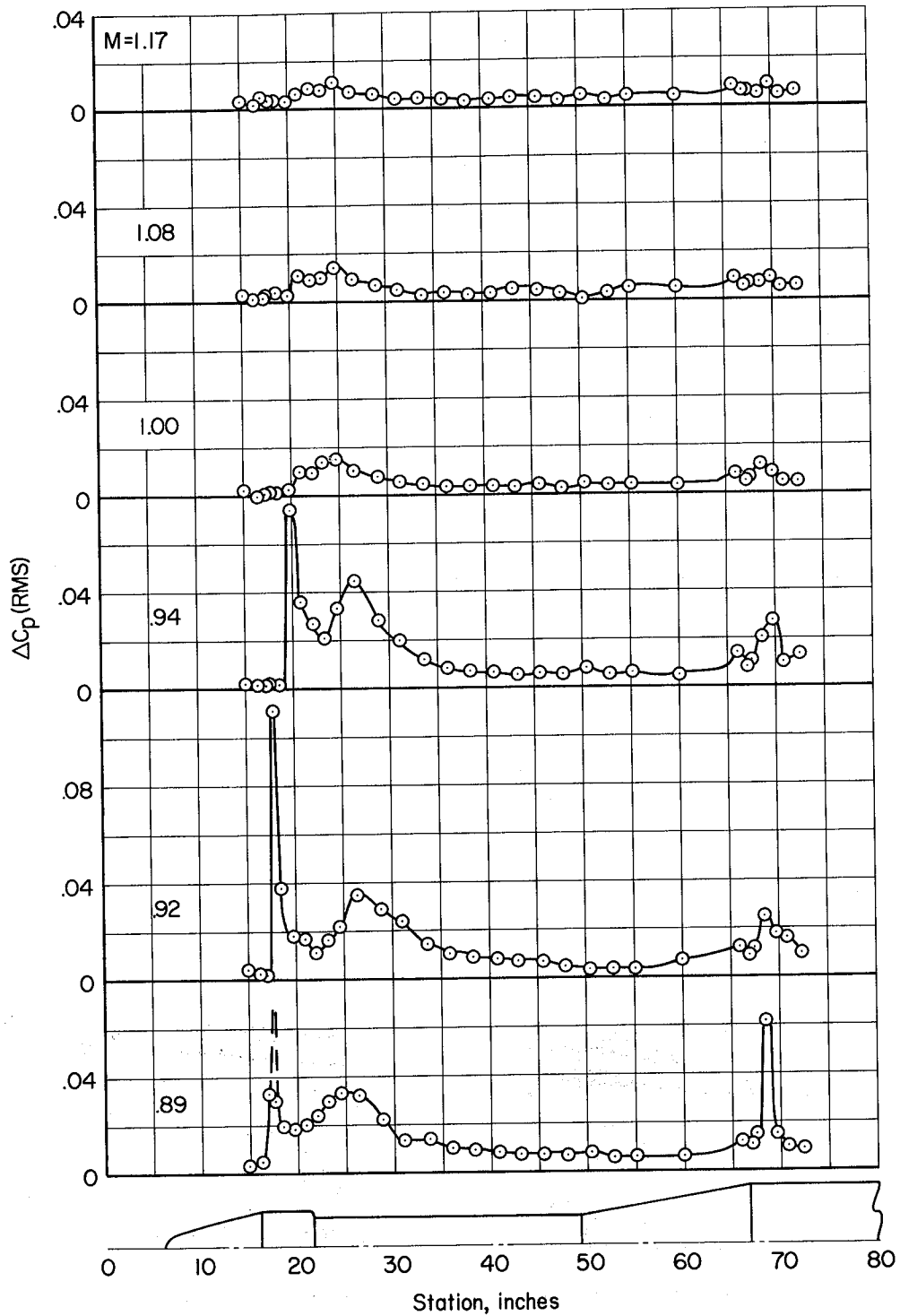




(d) $\alpha = 8^\circ$

Figure 8.- Continued.





(d) $\alpha = 8^\circ$ - Concluded.

Figure 8.- Concluded.



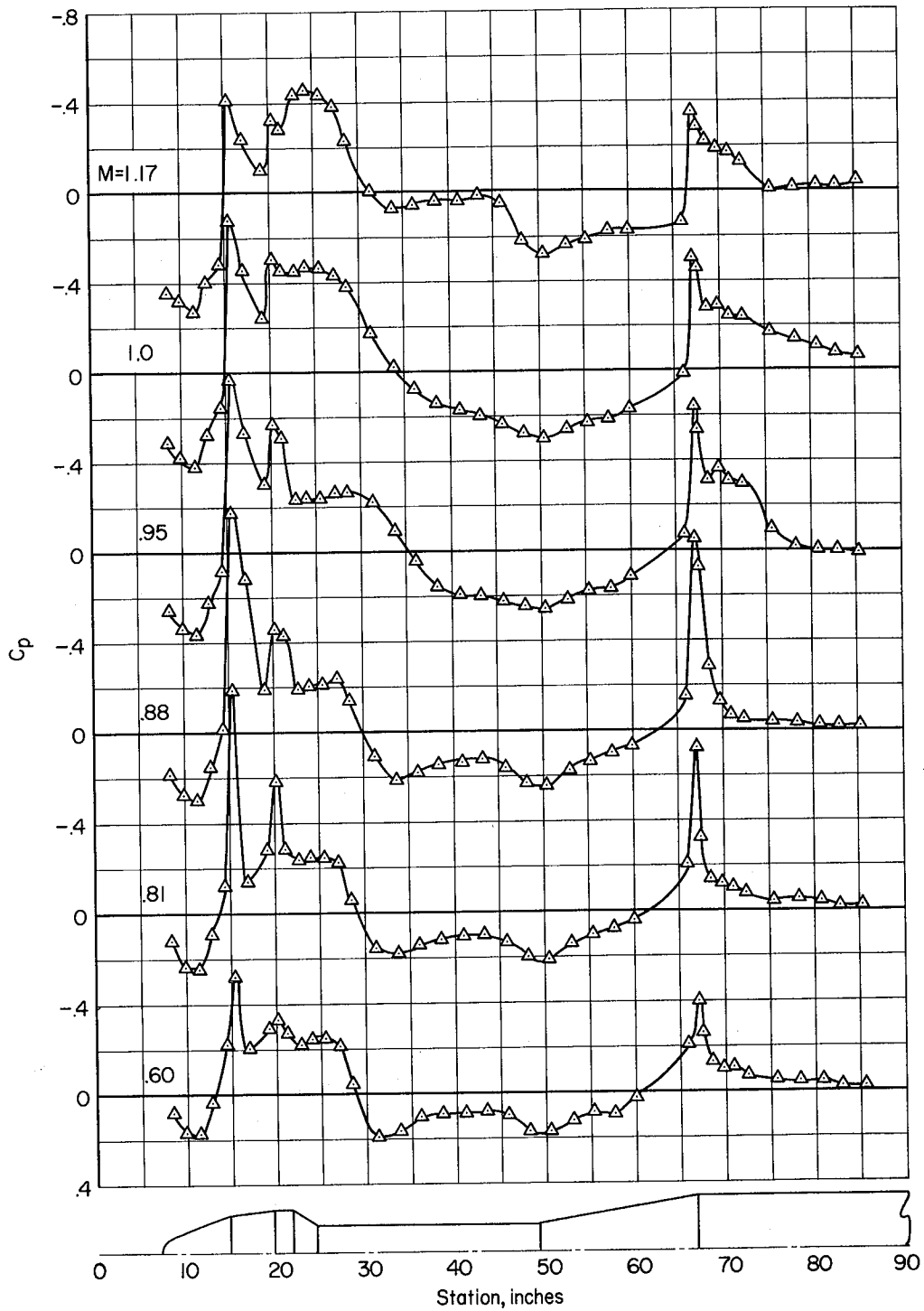
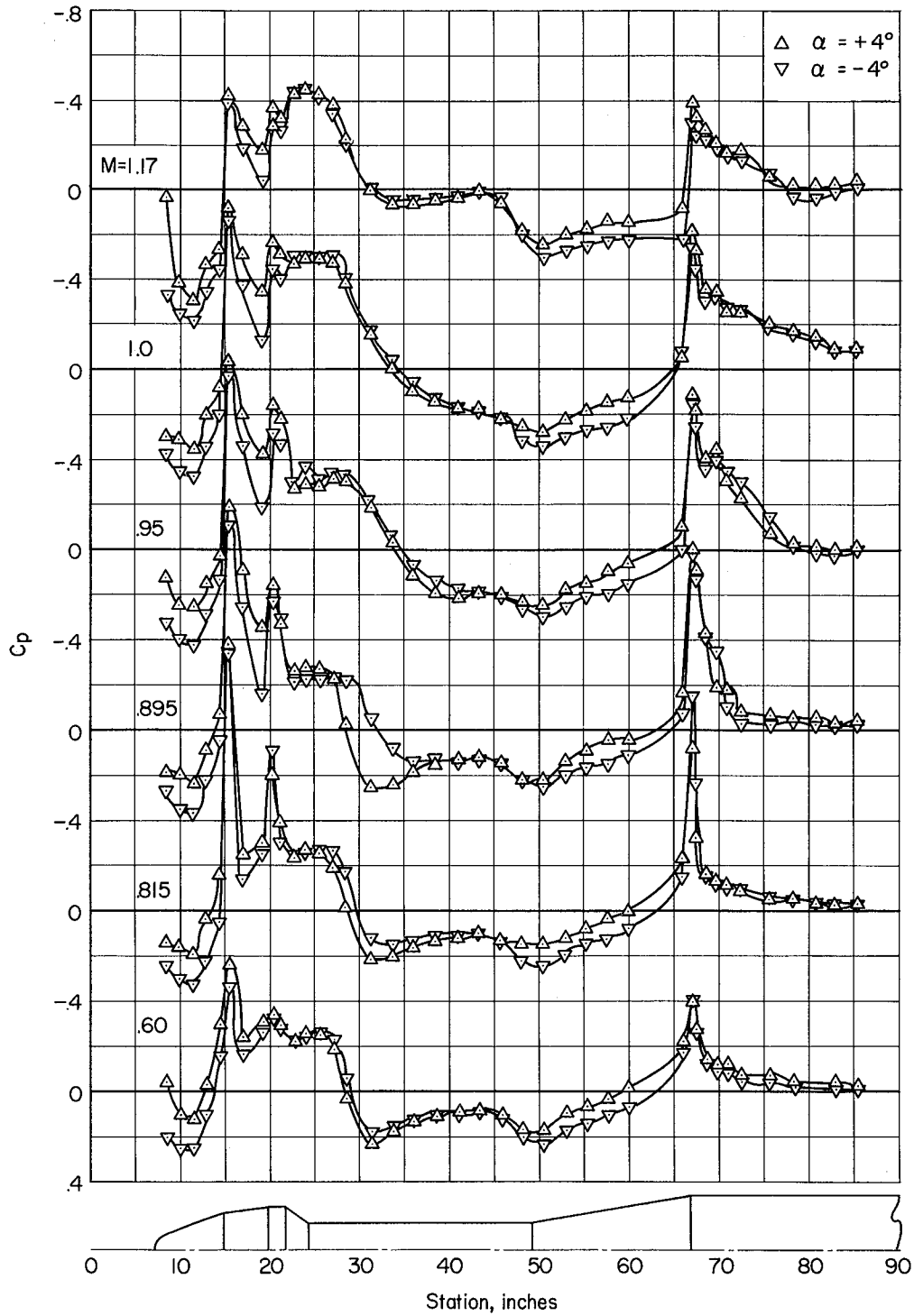
(a) $\alpha = 0^\circ$

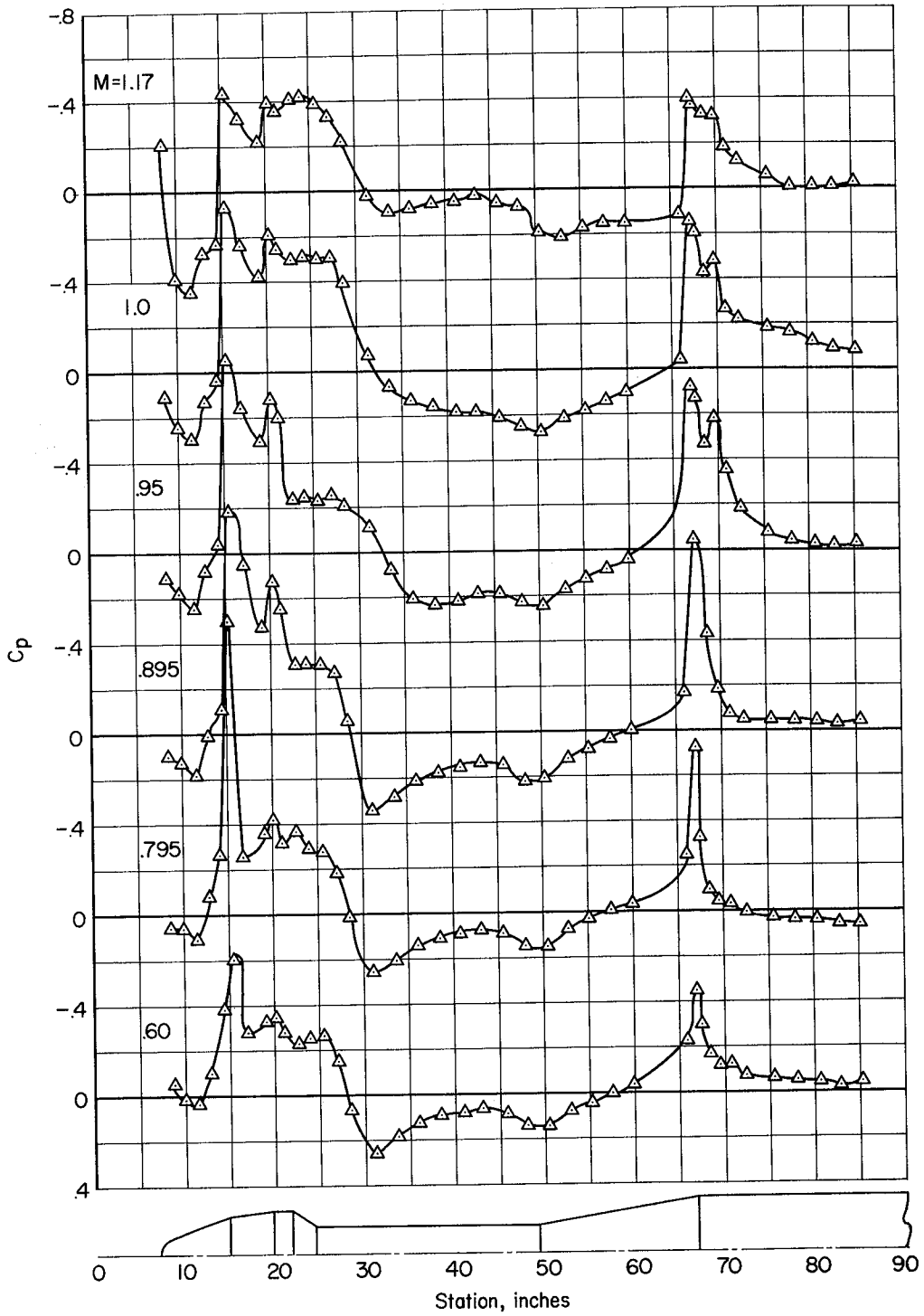
Figure 9.- Time-average static pressure distribution on the model 11.



(b) $\alpha = \pm 4^\circ$

Figure 9.- Continued.

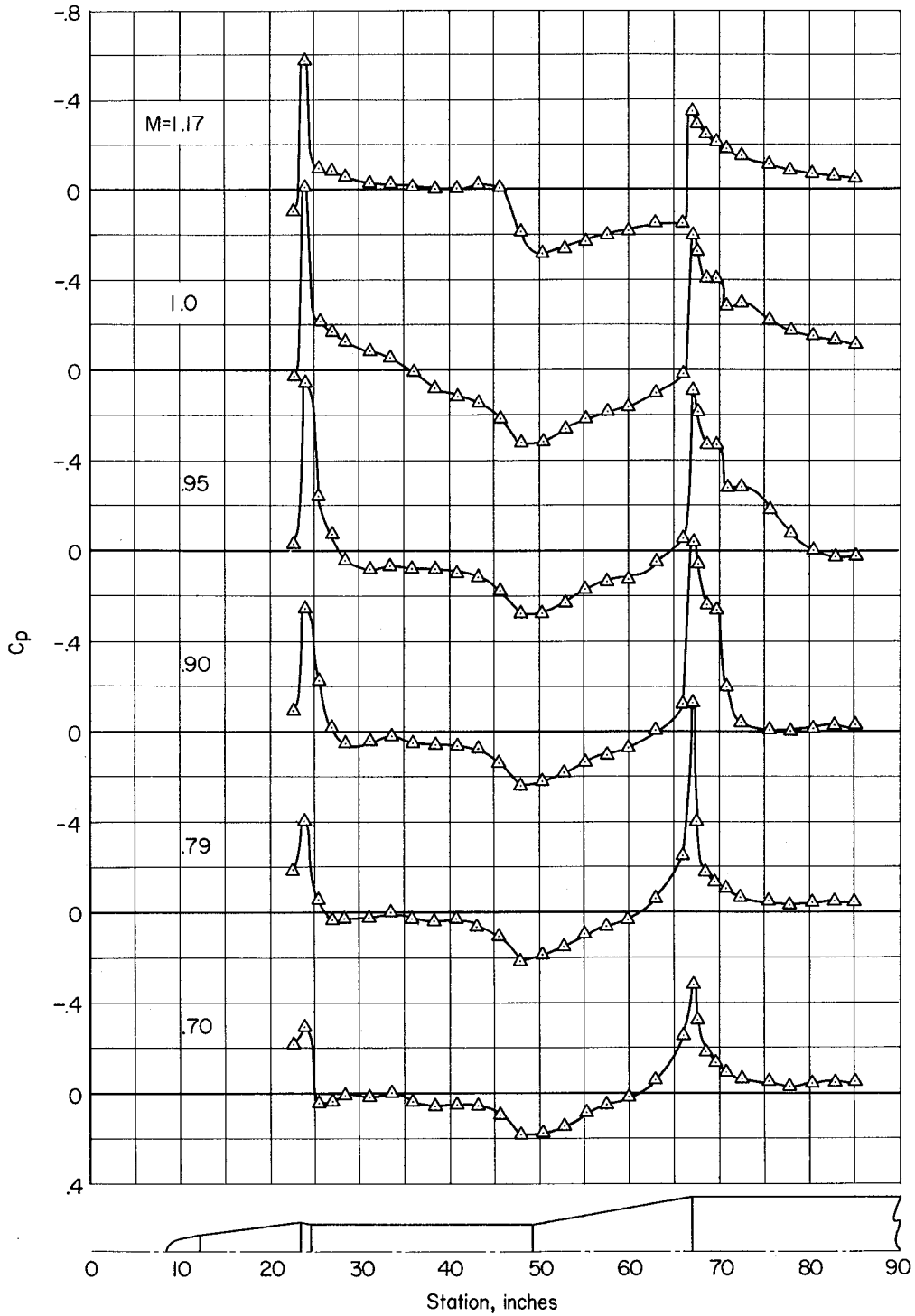




(c) $\alpha = 8^\circ$

Figure 9.- Concluded.

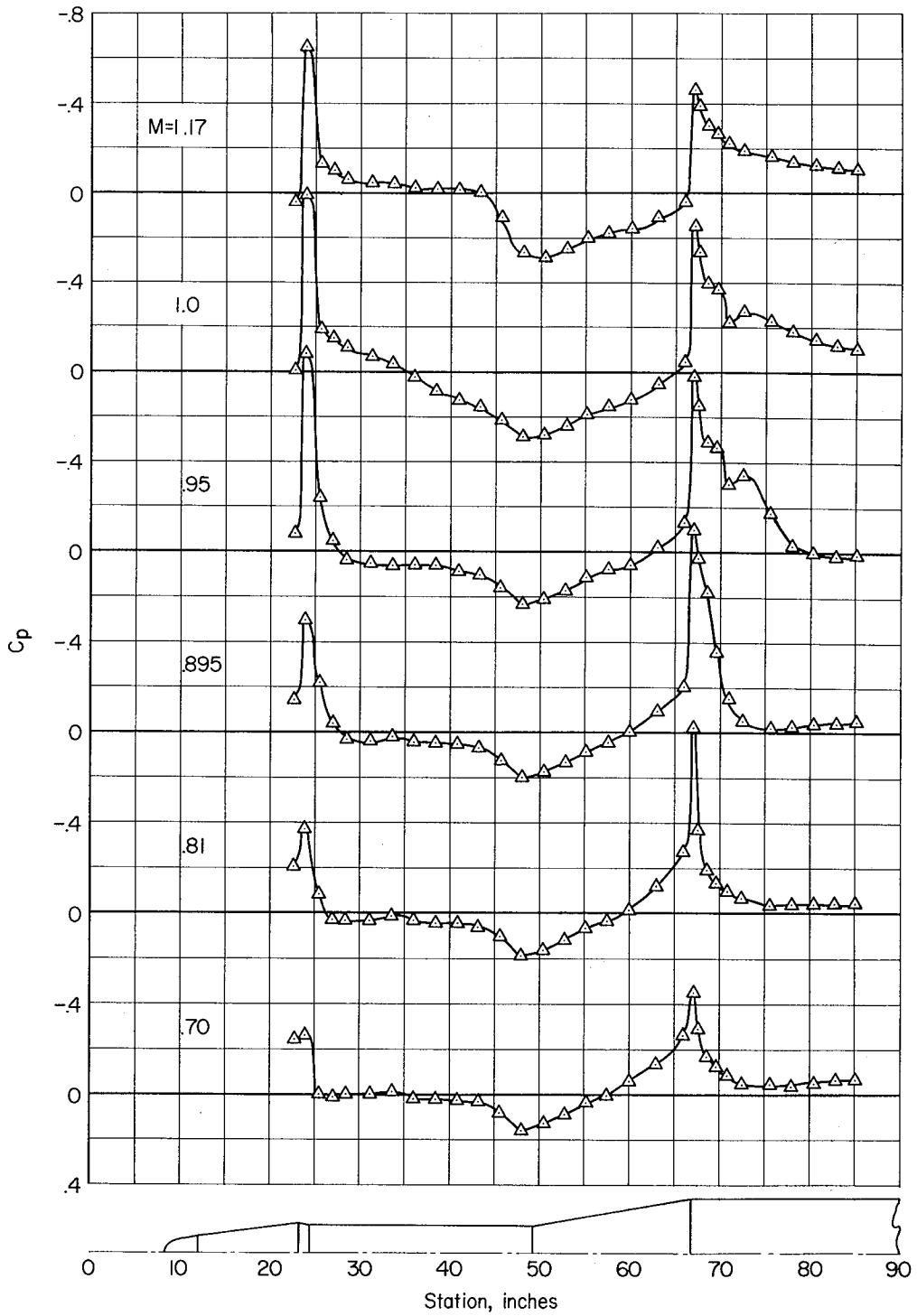




(a) $\alpha = 0^\circ$

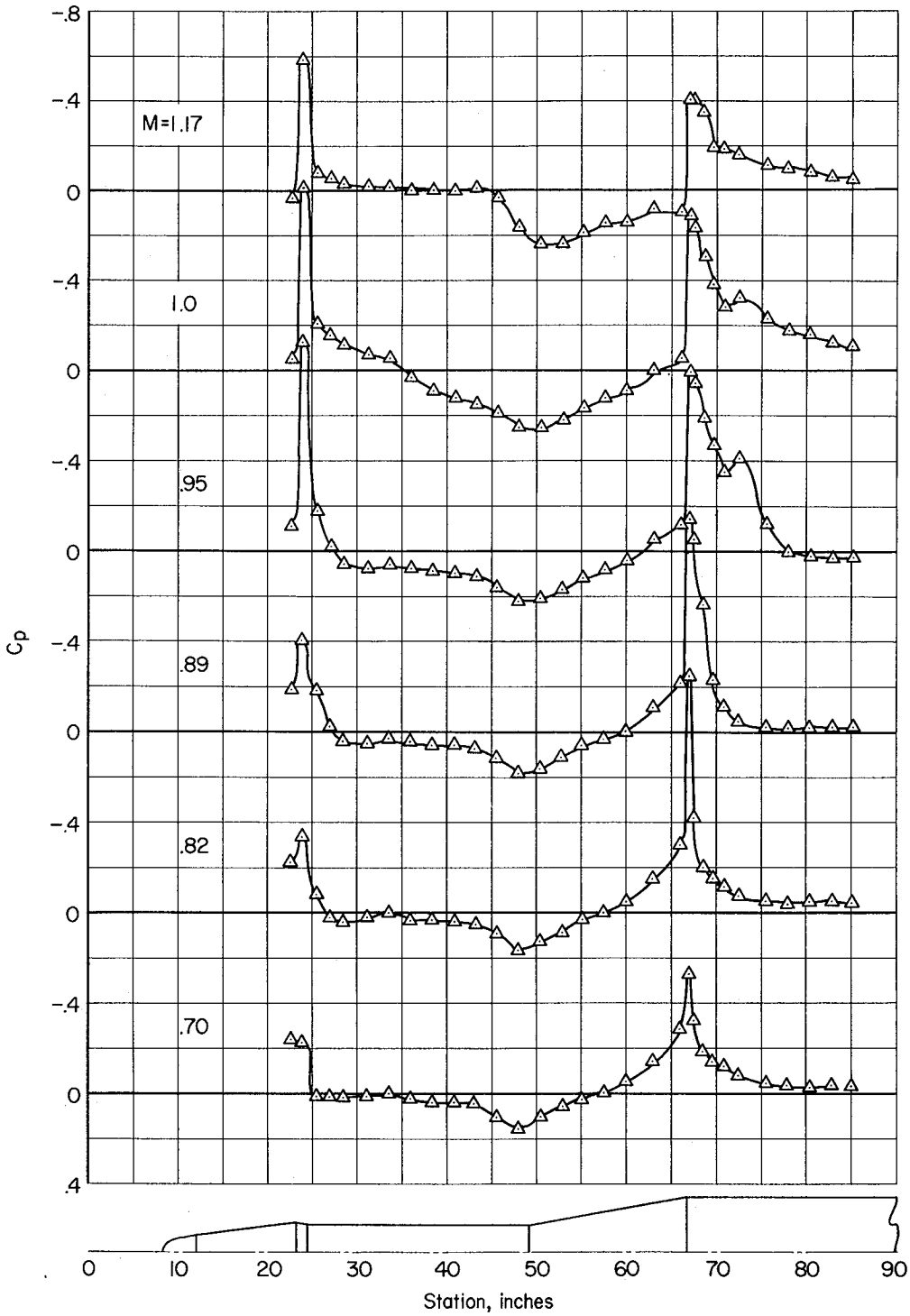
Figure 10.- Time-average static pressure distributions on model 12.





(b) $\alpha = 4^\circ$

Figure 10.- Continued.



(c) $\alpha = 8^\circ$

Figure 10.- Concluded.



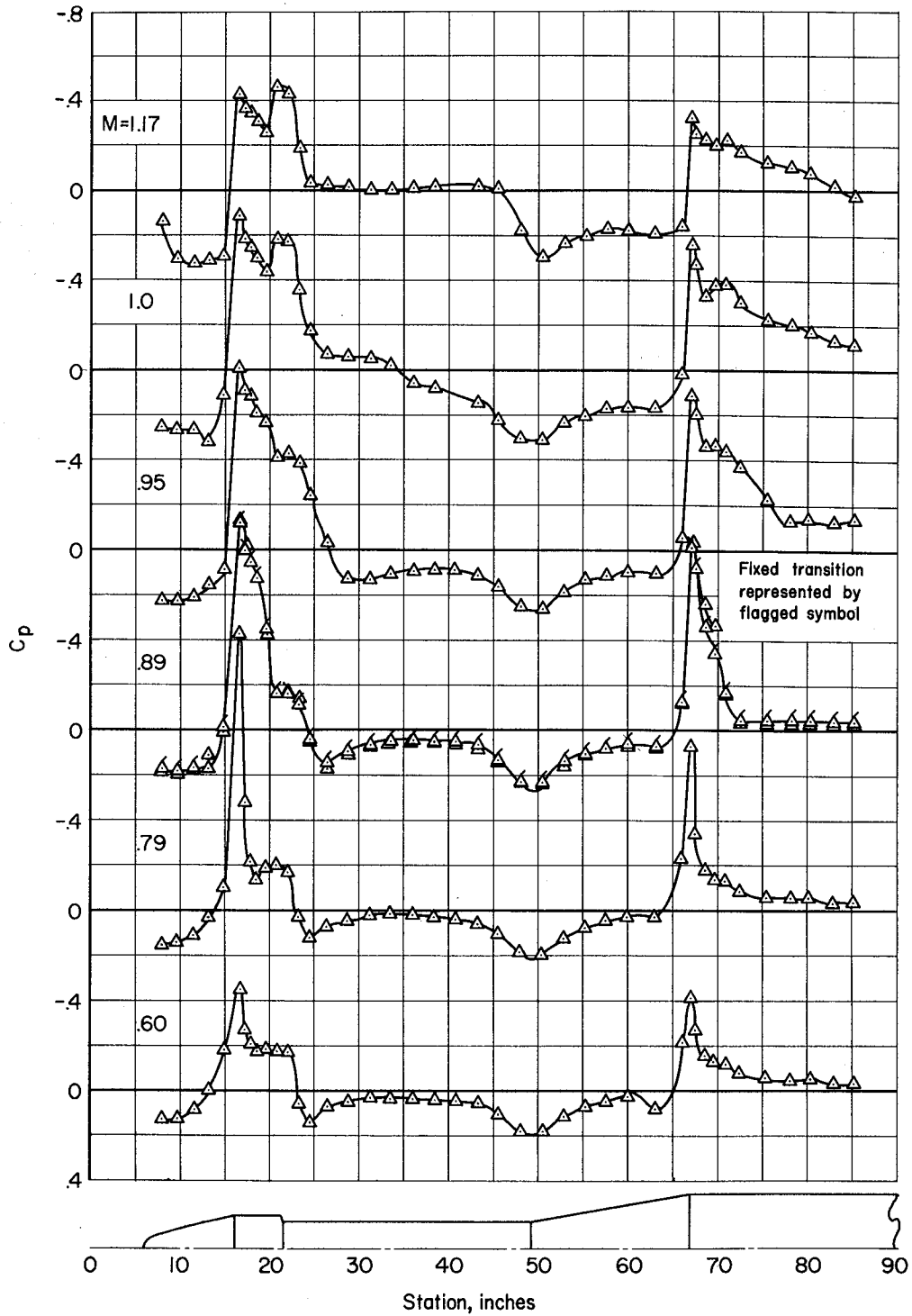
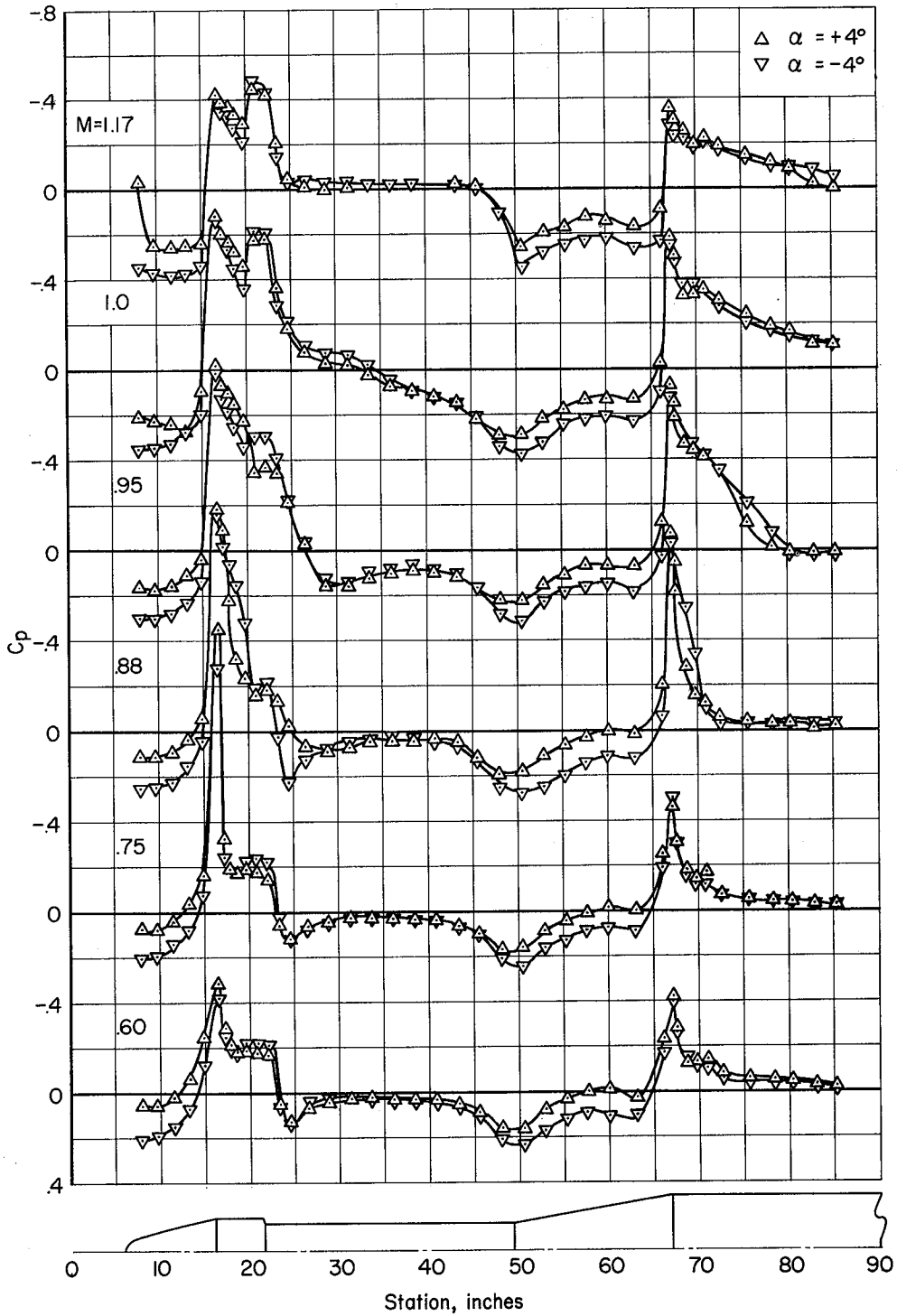
(a) $\alpha = 0^\circ$

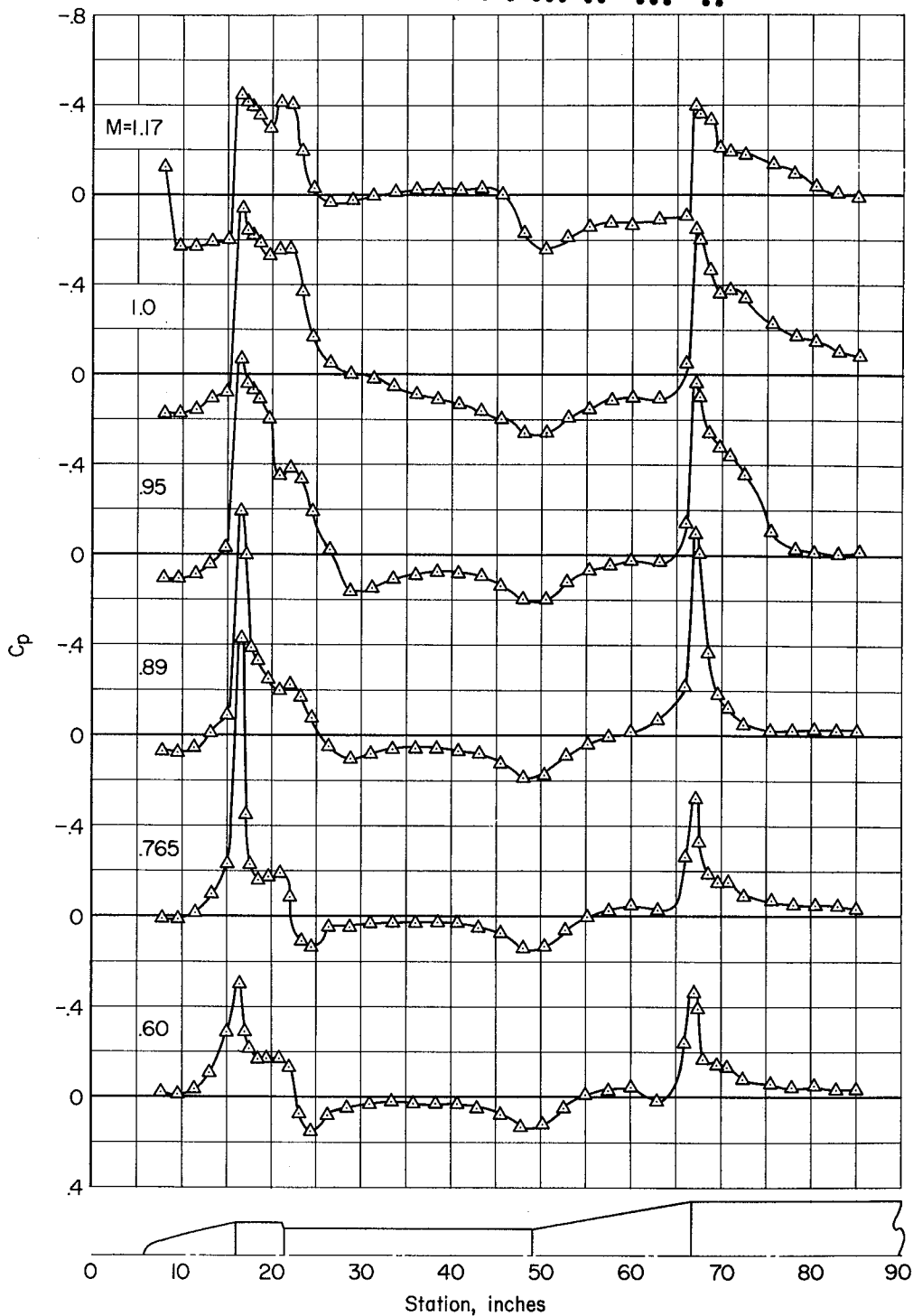
Figure 11.- Time-average static pressure distributions on model 13.



(b) $\alpha = \pm 4^\circ$

Figure 11.- Continued.

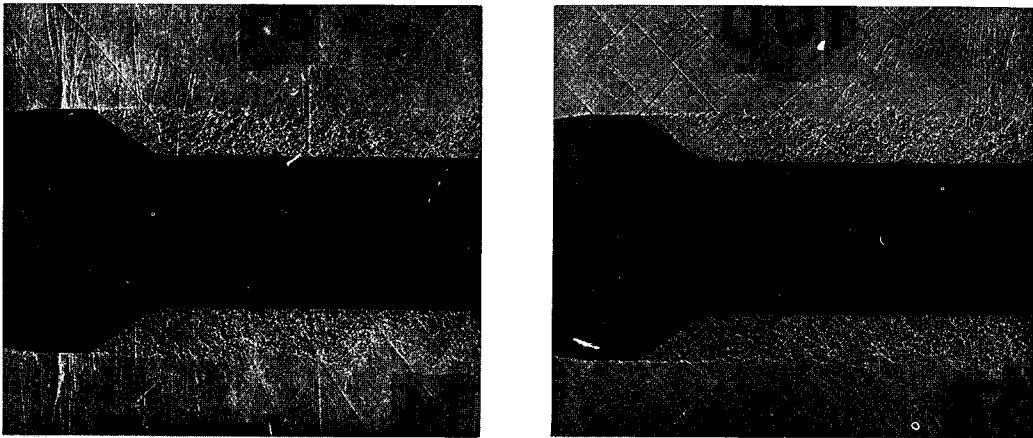
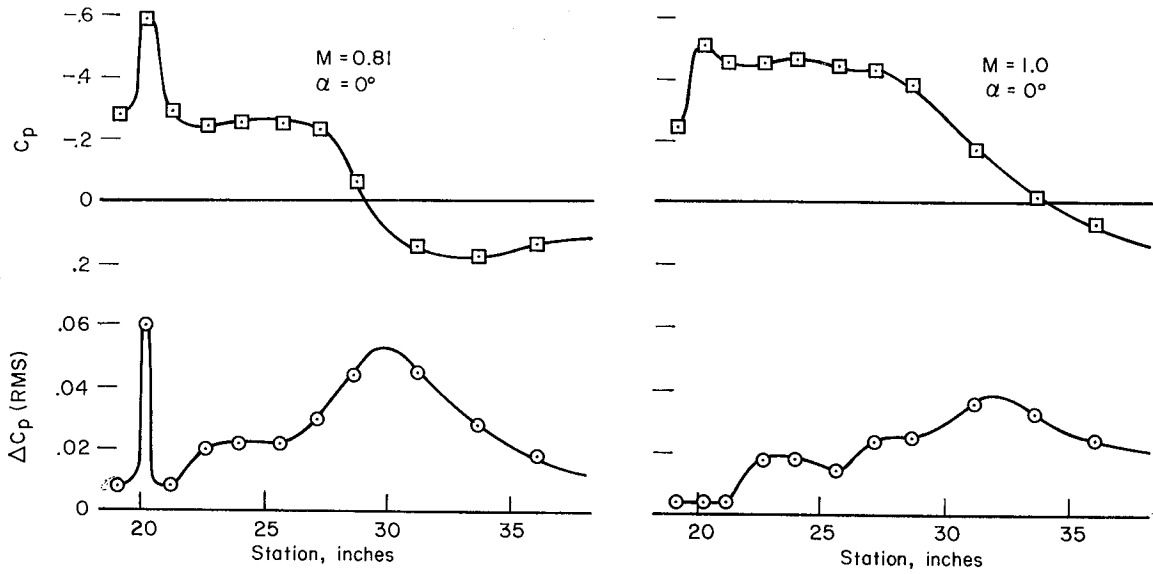




(c) $\alpha = 8^\circ$

Figure 11.- Concluded.

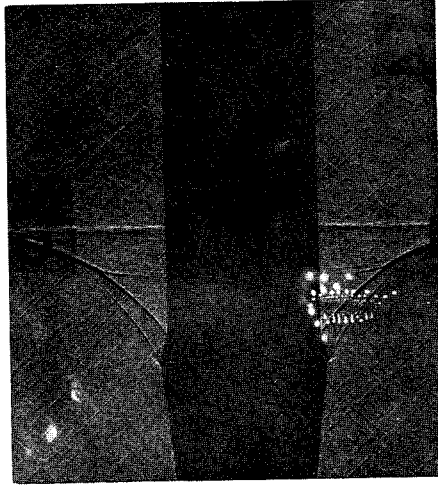
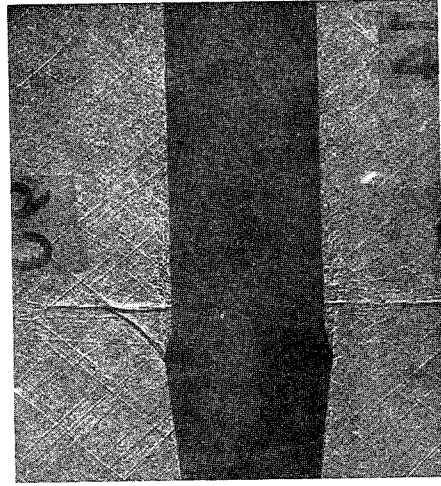
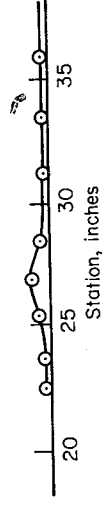
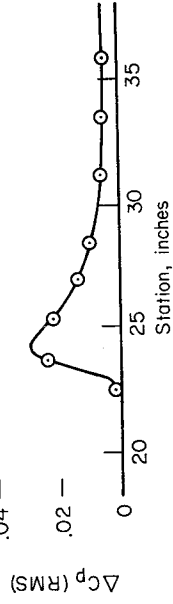
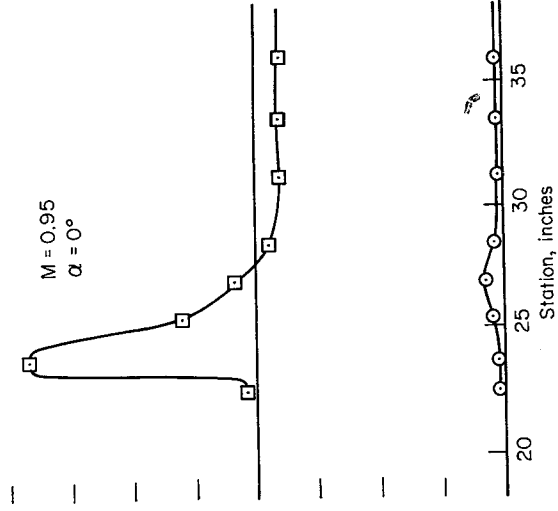
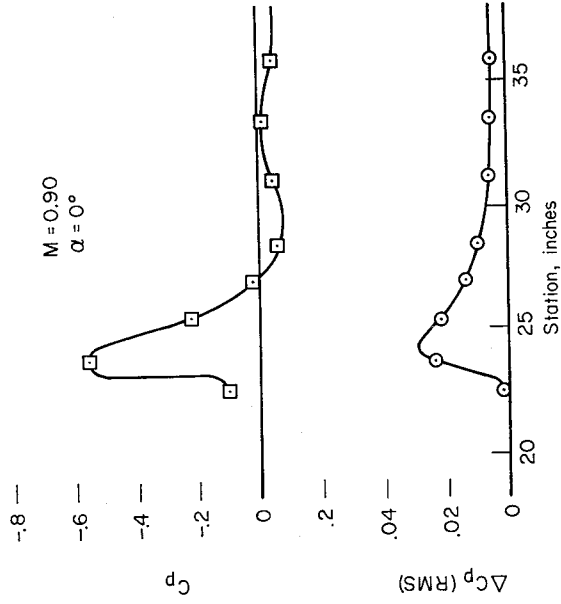




(a) Model 11

Figure 12.- Representative comparisons between steady and fluctuating pressure distributions and shadowgraph pictures of the models.

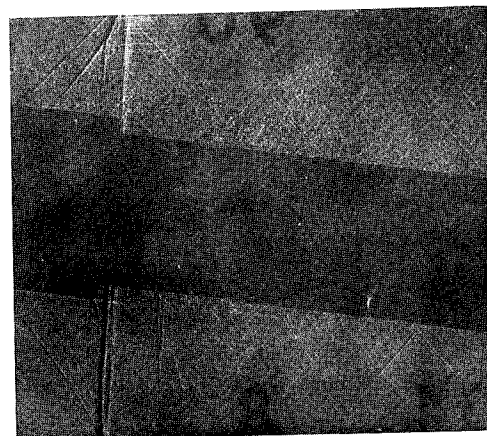
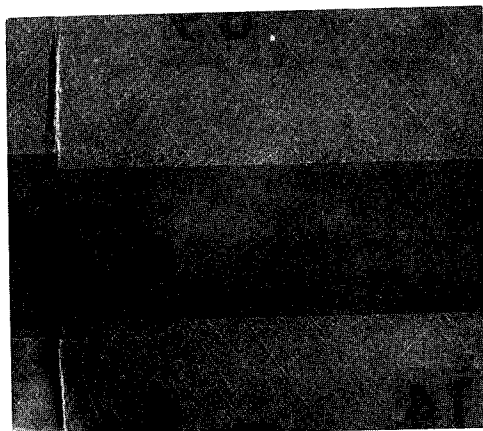
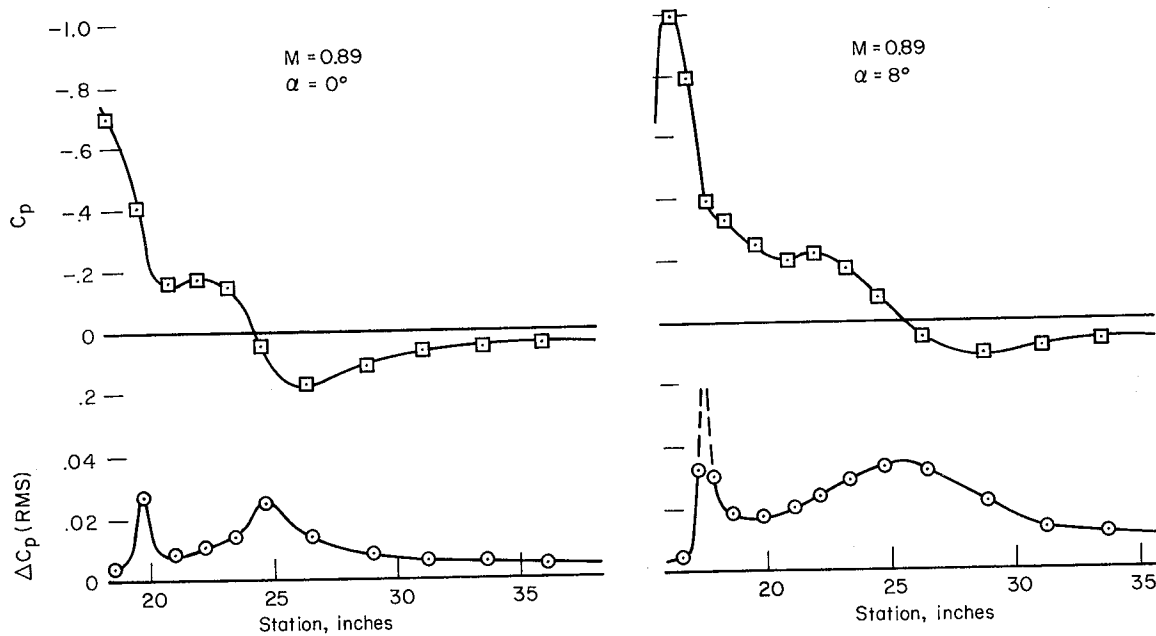
CONFIDENTIAL



(b) Model 12

Figure 12.- Continued.





(c) Model 13

Figure 12.- Concluded.

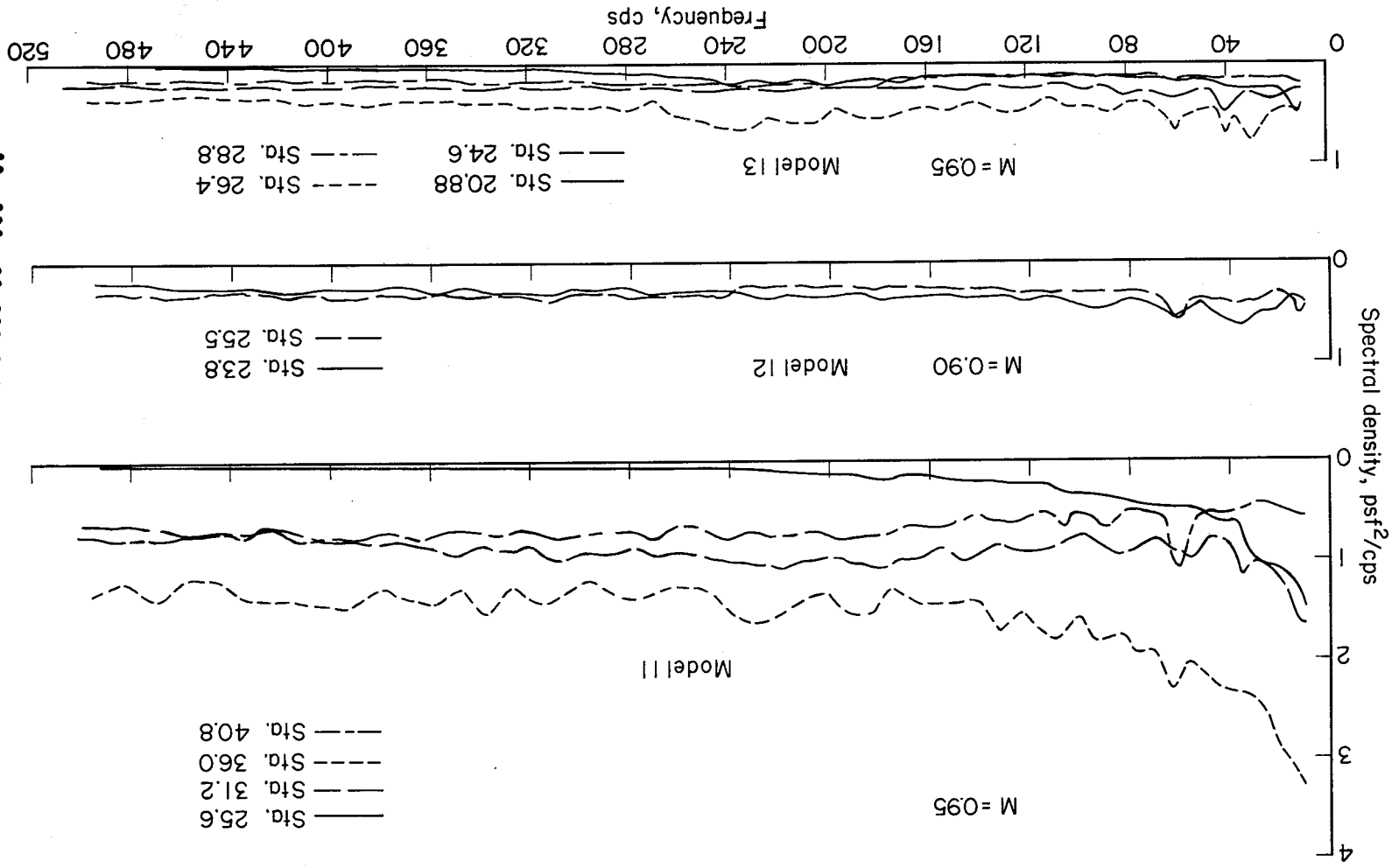


Figure 13.- Representative power spectra of pressure fluctuations in the separated regions on the models at $\alpha = 0^\circ$.

CONFIDENTIAL